Final Report
for
Air Force Research Laboratory
Aerospace Systems Directorate

Design Optimization of Slotted Waveguide Antenna Stiffened Structures

Date:	8 January 2014
Desired Initial Funding Period:	1 Jan 2011–31 Dec 2013
Proposed Duration of Project:	36 Months
Principal Investigator:	Robert A. Canfield

Aerospace and Ocean Engineering Department
Virginia Polytechnic Institute and State University
214 Randolph Hall
Blacksburg, VA 24061
(540) 231-5981
bob.canfield@vt.edu

REPORT DOCUMENTATION PAGE

Form Approved
OMB No. 0704-0188

1. REPORT DATE *(DD-MM-YYYY)*	**2. REPORT TYPE**	**3. DATES COVERED** *(From - To)*
08-01-2014	Final Technical Report	1 Jan 2011–31 Dec 2013

4. TITLE AND SUBTITLE

Title: AFRL-VT-WSU Collaborative Center on Multidisciplinary Sciences
Subtitle: Design Optimization of Slotted Waveguide Antenna Stiffened Structures (SWASS)

5a. CONTRACT NUMBER
FA8650-09-2-3938

5b. GRANT NUMBER

5c. PROGRAM ELEMENT NUMBER

6. AUTHOR(S)

Kim, Woon Kyung, Postdoc, Virginia Tech

Canfield, Robert A., Professor, Virginia Tech

5d. PROJECT NUMBER

5e. TASK NUMBER

5f. WORK UNIT NUMBER

7. PERFORMING ORGANIZATION NAME(S) AND ADDRESS(ES)

Aerospace and Ocean Engineering (MC0203)
Randolph Hall, RM 215, Virginia Tech

8. PERFORMING ORGANIZATION REPORT NUMBER

VT-AOE-13-002

9. SPONSORING / MONITORING AGENCY NAME(S) AND ADDRESS(ES)

William Baron, and James Tuss
Aerospace Systems Directorate, AFRL, WPAFB,OH

10. SPONSOR/MONITOR'S ACRONYM(S)

11. SPONSOR/MONITOR'S REPORT NUMBER(S)

12. DISTRIBUTION / AVAILABILITY STATEMENT

APPROVED FOR PUBLIC RELEASE; DISTRIBUTION UNLIMITED.

13. SUPPLEMENTARY NOTES

14. ABSTRACT

The objective of the research is to investigate computational methods for design optimization of a Conformal Load-Bearing Antenna Structure (CLAS) concept. Research centers on investigating computational methods for design optimization of a slotted waveguide antenna stiffened structure (SWASS). The goal of this concept is to turn the skin of aircraft into a radio frequency (RF) antenna. SWASS is a multidisciplinary blending of RF slotted waveguide technology and stiffened composite structures technology. Waveguides provide channels for RF signal transmission, as well as structural stiffening. A SWASS skin or stiffener will have numerous slots that allow the RF energy to radiate to the atmosphere. Slot design for maximum RF performance with minimum structural performance degradation due to the slots will be the multidisciplinary, multiobjective design challenge. Initially, waveguides acting as hat stiffeners were considered in this research; then, waveguides that constituted the core of a sandwich panel were designed for loads in the aircraft skin. The concept design requires parameterization of slot shape, size, location, and spacing in conjunction with stiffener or core sizing and spacing, composite material selection, and laminate layout in order to simultaneously meet desired structural and RF performance.

15. SUBJECT TERMS

SWASS, CLAS, slotted waveguide, response surface methodology, multifunctional composite structure, SORCER

16. SECURITY CLASSIFICATION OF:			**17. LIMITATION OF ABSTRACT**	**18. NUMBER OF PAGES**	**19a. NAME OF RESPONSIBLE PERSON**
a. REPORT	**b. ABSTRACT**	**c. THIS PAGE**			Robert A. Canfield
U	U	U	UU	69	**19b. TELEPHONE NUMBER** *(include area code)* 540-231-5981

Standard Form 298 (Rev. 8-98)
Prescribed by ANSI Std. Z39.18

Executive Summary

Title: Design Optimization of Slotted Waveguide Antenna Stiffened Structures (SWASS)

Principal Investigator: Dr. Robert A. Canfield

Research Objectives:

- Verify multi-fidelity models of SWASS waveguide tubes for both electromagnetic (EM) and structural performance. Validate structural finite element model (FEM) against experimental results.
- Quantify the tradeoff between structural and RF performance for characteristic integrated SWASS design concepts. Formulate multidisciplinary analysis and design optimization problem for SWASS using finite element meshes based on common geometry.
- Deliver computational models and source for SWASS design optimization that is compatible and functions with Service ORiented Computing EnviRonment (SORCER).

Synopsis of Research: The objective of the research is to investigate computational methods for design optimization of a Conformal Load-Bearing Antenna Structure (CLAS) concept. Research centers on investigating computational methods for design optimization of a slotted waveguide antenna stiffened structure (SWASS). The goal of this concept is to turn the skin of aircraft into a radio frequency (RF) antenna. SWASS is a multidisciplinary blending of RF slotted waveguide technology and stiffened composite structures technology. Waveguides provide channels for RF signal transmission, as well as structural stiffening. A SWASS skin or stiffener will have numerous slots that allow the RF energy to radiate to the atmosphere. Slot design for maximum RF performance with minimum structural performance degradation due to the slots will be the multidisciplinary, multiobjective design challenge. Initially, waveguides acting as hat stiffeners were considered in this research; then, waveguides that constituted the core of a sandwich panel were designed for loads in the aircraft skin. The concept design requires parameterization of slot shape, size, location, and spacing in conjunction with stiffener or core sizing and spacing, composite material selection, and laminate layout in order to simultaneously meet desired structural and RF performance.

Table of Contents

List of Figures

List of Tables

Chapter 1 Introduction

1.1 Objectives

Existing antennas are attached to an aircraft surface as blades or enclosed within the aircraft structure, typically covered by electromagnetically transparent and structurally weak composite materials such as fiberglass. In contrast, conformal antennas may be integrated into the honeycomb core, stiffeners or the skin of aircraft surface panels. In the case of a waveguide structure, the size can be bigger than antennas that are located on the surface of the fuselage. Therefore, it can bear more internal or external forces than other antenna structures. Since this new concept antenna structure can be installed in the main part of load bearing structures, it will perform the roles of a structure and an antenna. The goal is to use Multidisciplinary Design Optimization (MDO) to achieve high structural performance, such as the strength or stiffness, and simultaneously maintain antenna characteristics, such as the gain or beam pattern. Ultimately, the research objective is to quantify the synergistic benefit of simultaneous structural and RF design of SWASS.

1.2 Air Force Relevance

Airframe structures have been developed historically from a fabric covered wood, later from aluminum skin and stringer frame, and now more frequently from high modulus composite [1]. Most Radio Frequency (RF) engineers are interested in designing antennas and radomes independently, and then they try to resolve the interface problems. However, the opportunity exists to pursue a novel technology to structurally integrate antennas.

The most common benefit of the structurally integrated antenna is drag reduction [2]. Large antenna structures, such as reflecting dishes or planar arrays that cause drag, are mounted in fairings or radomes of existing aircraft. An opportunity exists for structurally integrated antennas to replace many protruding antennas. In addition, removing external antennas can reduce radar cross section (RCS) of an aircraft. There are many other merits besides reducing the RCS of an aircraft. External antennas such as blades can be damaged, when objects pass close to the aircraft outer mold line (OML) [2] and contact the antennas. They are subject to impact in flight operation, ground handling, and maintenance. Specifically, fixed wing aircraft might fly through inclement weather such as hailstorm or gust, and rotorcraft might contact foliage or objects when operating from a harsh helipad. Moreover, an aircraft can obtain more lift force by adopting structurally embedded antennas [2]. Since the antenna is usually bulky, if it is incorporated into other components, good aerodynamic performance can be achieved.

1.3 Background

A few programs such as Conformal Load-Bearing Antenna Structure (CLAS) [2], Smart Skin Structures Technology Demonstration (S3TD) [3], and RF Multifunction Structural Aperture (MUSTRAP) [4] strove to advance the technology of integrating structures and antennas to produce higher efficiency of the design and maintenance. Significant contributions of these programs are a weight saving and drag reduction. At the Air Force Institute of Technology (AFIT) Smallwood, Canfield and Terzoulli studied a structurally integrated antenna mounted into the wings of a joined-wing aircraft [5]. Recently, high frequency microstrip antennas embedded in aircraft skin were examined [6]. The microstrip patch antenna was installed to a space between a facesheet and a honeycomb structure.

1.3.1 Structurally Integrated Antennas on a Joined-Wing Aircraft

The AFIT research sought to study a concept that embeds conformal load-bearing antenna arrays into the wing structure of a joined-wing aircraft [5]. Because the wings deform under the flight condition, it could affect the original configuration of the antenna. Therefore, the effect in antenna performance was measured against wing deformation. Smallwood *et al* [5] used half-wavelength dipoles to model the conformal load-bearing antenna element and a commercial software package, NEC-Win Plus+^{TM} using the Method of Moments solution technique, to prove the analytic model. A simple model of the sensors was generated to integrate the different layers of materials to construct antenna's structure. A simplified finite element model of antenna consisted of five layers, which were an electromagnetically transparent material called Astroquartz, two honeycomb core structures, and two graphite epoxy layers. Astroquartz and graphite epoxy are modeled as symmetric composite layers with 0^o, $+/-45^o$, and 90^o plies. Wing deformations were generated on a fully stressed design by an integrated software environment using the Adaptive Modeling Language (AML), MSC.NASTRAN, and PanAir. These deformations were used to locate the new position and slope of each element of array. Then, a new beam pattern was generated. They repeated this process for the various load configurations. Baseline results and repeated process results were compared to determine the beam pointing error due to the wing deformations.

NEC-Win Plus+^{TM} and dipole theory implemented in MATLAB were used to produce radiation patterns on the undeformed and deformed wing. The radiation pattern of 10x40 element array located close to the fuselage, depicted in Figure 1.1, was calculated for the undeformed and deformed wing under the gust load. Results from each method were compared in Figure 1.2 and Figure 1.3. The overall patterns showed some similarities, but the array theory patterns were wider than the NEC patterns. For a deformed wing due to a steady 2.5g maneuver load and a gust load, the radiation pattern was affected by the deformation, but the azimuth angles were essentially the same. The worst pointing error of approximately 9^o occurred for a gust load condition.

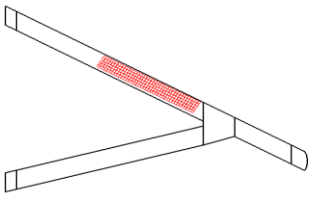

Figure 1.1. 10x40 element array located on the front wing section [5]

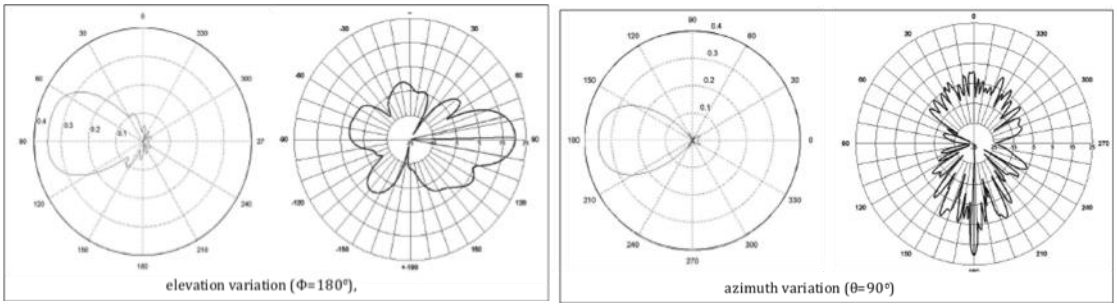

Figure 1.2. Magnitude of E-field radiation in [V/M] from 10x40 arrays on undeformed wing : Left-MATLAB plots, Right-NEC plots [5]

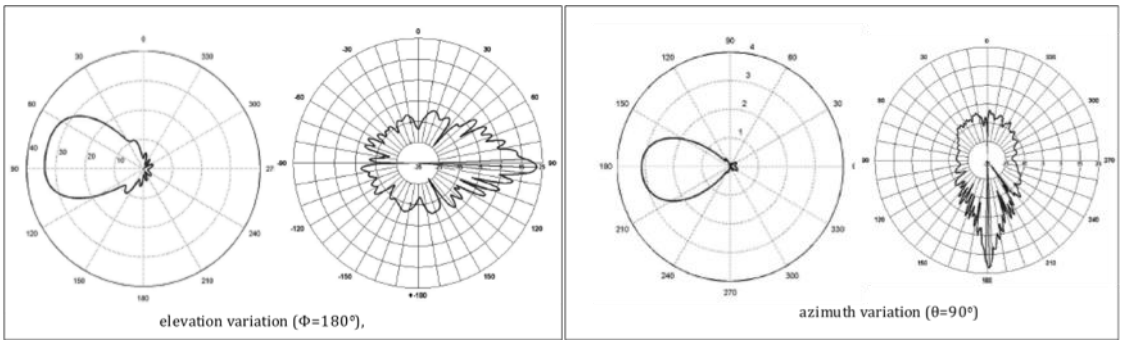

Figure 1.3. Magnitude of E-field radiation in [V/M] from 10x40 arrays on deformed wing for gust

1.3.2 Aircraft X-Band Radar

Every aircraft has an electronic device for radio detecting and ranging (radar). Radar radiates electromagnetic waves to detect far off objects such as aircraft, ships, and buildings, and recognize them by the reflecting echo from the objects. In other words, aircraft radar can be compared to a major visual center of a pilot in the sky. In addition, radar is not only used for satellite communication but also to control military weapons [7].

The microwave band was divided into narrow bands and allocated letters for purpose of military security: L, S, C, X, and K-band. Compared to the higher frequencies, the hardware is larger for the lower frequencies, since the wavelengths are long. Higher frequencies have a higher limitation on the power transmission. Nevertheless, microwave devices have some merits. Firstly, they can focus a narrow beam to detect targets accurately. The power can be accordingly concentrated in a particular direction. Secondly, microwaves pass through the atmosphere with low attenuation of absorption and scattering due to water vapors or raindrops. Below about 0.1 GHz, the atmospheric attenuation such as absorption and scattering is negligible, but it becomes significant beyond 10 GHz. Lastly, ambient noise is gradually decreased from L-band to X-Band, but it become increasingly higher than K-band [8]. For those reasons, X-band radar systems of 8 to 12.5 GHz are usually used for fighter aircraft. For example, F-14, F-15, F-16, and F/A-18 use X-band radar systems such as AN/APG-63, 65, 68, 70, 71 and 73 [9].

Waveguide components may replace lumped circuit elements in the frequency from 1 to 100 GHz. Because radar typically uses microwave frequencies, waveguide antennas are good airborne radar antennas for satellite communication, detecting targets, and missile-tracking or guidance radar [10]. The waveguide antenna frequency of this research will be focused at 10 GHz frequency in the X-band.

1.3.3 Electromagnetic Performance for Waveguides

The gain is defined as

$$G = 4\pi \frac{U(\theta,\phi)}{P_{in}} \tag{1.1}$$

where P_{in} is the total input power and $U(\theta,\phi)$ is the radiation intensity [11]. Beamwidth is the configuration of the mainlobe. There are two types of beamwidth characterization. One is the half-power beamwidth (HPBW) and another one is first-null beamwidth (FNBW), shown in

Figure 1.4 [11]. Those are determined by the slotted waveguide design. The slot shape and dimension yield the desired radiation pattern. The antenna size determines the frequency of the radiation. In addition, the frequency depends on the cross sectional shape and dimension of the waveguide antenna [12]. The frequency is determined as

$$f = \frac{\lambda}{c} \tag{1.2}$$

where f is the frequency, λ is the wavelength, and c is the speed of light. Also, cut-off frequency, which is the minimum frequency to propagate waves, is

$$f_c = \frac{c}{2\sqrt{\mu\varepsilon}}\sqrt{\left(\frac{m}{a}\right)^2 + \left(\frac{n}{b}\right)^2} \tag{1.3}$$

in which a is the width of the rectangular waveguide, b is the height of the rectangular waveguide shown in Figure 1.5, ε is the dielectric constant, μ is the magnetic permeability within the waveguide, m and n are the numbers of the mode variations for transverse electric (TE) or transverse magnetic (TM) waves [13].

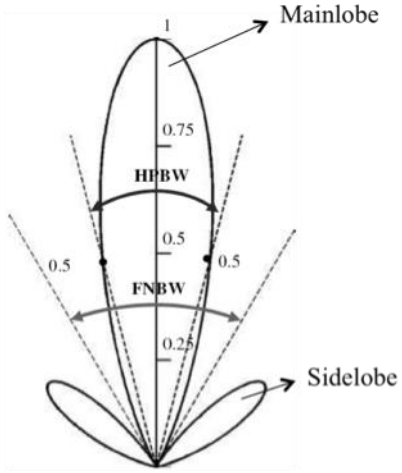

Figure 1.4. A half-power beamwidth (HPBW) and a first-null beamwidth (FNBW) [11]

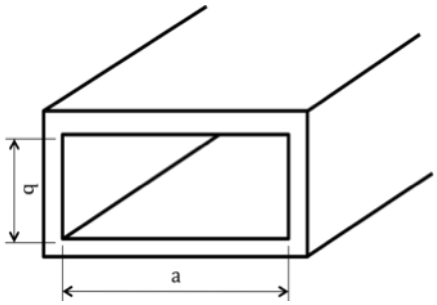

Figure 1.5. Rectangular waveguide

1.3.4 Structural Analysis and Design

In the case of the structures, optimum designs must consider local and global buckling, ultimate strength of tension and compression, strain, and so on [14]. The stability of structures such as local buckling will be considered, since stiffeners, such as those shown in Figure 1.6,

may reach the local buckling load prior to the ultimate strength. When panel buckling occurs, it may affect the electromagnetic waves due to the variation of the waveguide antenna section. The critical stress of panel buckling, $(\sigma_x)_{cr}$, with four edges of a rectangular plate simply supported under uniaxial loads is

$$(\sigma_x)_{cr} = \frac{\pi^2 D}{t_s a^2}(m + \frac{n^2}{m}\frac{a^2}{b^2})^2 \tag{1.4}$$

in which D is the flexural rigidity of an isotropic flat plate, $\frac{E_s t_s^3}{12(1-\nu_s^2)}$, E_s is the modulus of elasticity of the face sheet material, ν_s is the Poisson ratio of face sheet material, t_s is the thickness of face sheet, a is the length of global panel, b is the width of rectangular flat plate segment, m is the number of the buckle half-sine waves in x-direction, and n is the number of the buckle half-sine wave in y-direction, shown in Figure 1.7 [14]. Accordingly, the width of flange, the height of web, and the angle between the web and flange, shown in Figure 1.8, may be the design variables to optimize the hat-stiffened antenna structures. The waveguide slots might be placed on the broad wall surface or the side surface of the hat stiffeners in Figure 1.9. Slot shapes, shown in Figure 1.10, would be designed to make the intended radiation pattern [12].

The specific strength and specific modulus will be compared to conventional stiffeners. The specific strength is the ratio between the strength and the weight and the specific stiffness is the ration between the stiffness and the weight. The specific strength and specific modulus is

$$\text{Specific strength} = \frac{\sigma}{\rho} \tag{1.5}$$

$$\text{Specific modulus} = \frac{E}{\rho} \tag{1.6}$$

in which σ is the strength, ρ is the density, and E is the modulus of elasticity of the material.

Figure 1.6. Stiffened Structures: B-747 (left) and B-787 (right)

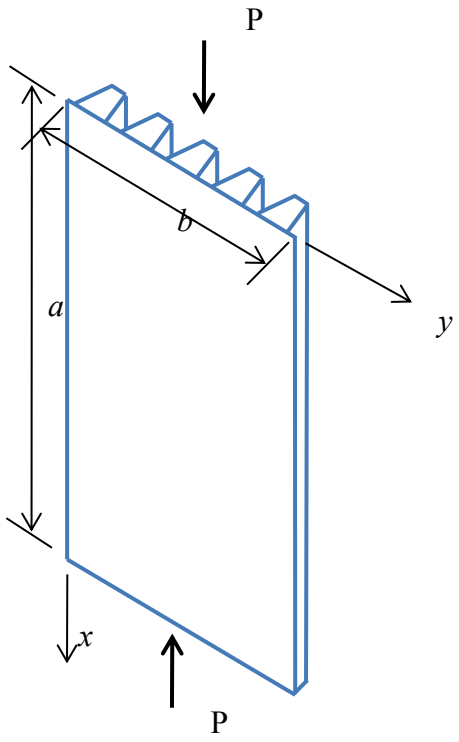

Figure 1.7. Hat-stiffened panel under uniaxial compression

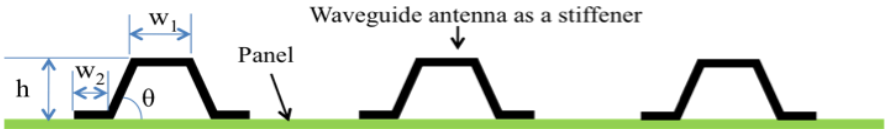

Figure 1.8. Hat shaped stiffened waveguide structures

Figure 1.9. Slots on the narrow wall (Left) and Slots on the broad wall (Right)

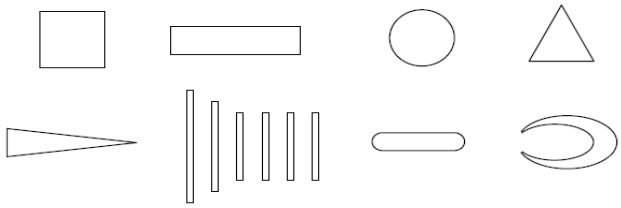

Figure 1.10. Slot shapes [12]

1.3.5 Software for Antenna Design

Techniques are classified as to whether they are solved in the time or frequency domain. Another classification is partial differential equation (PDE) or integral equation to solve the differential or integral form of Maxwell's equations. For example, Method of Moments (MoM) employs frequency domain and integral techniques; on the other hand FEM solves the discretized PDE's. Finite Difference Time Domain (FDTD) obviously uses is the time domain approach. Though MoM and FEM need a matrix solver to get solutions, FDTD does not require a matrix solver [15], because FDTD employs an explicit method.

The COMSOL Multiphysics FEM software simulates the physics with PDEs. It provides a number of predefined modeling interfaces for applications from fluid flow and heat transfer to structural mechanics and electromagnetic analysis. Specific modules contribute material libraries, solvers and elements. There are some modules to provide specific interfaces, includingand RF Module and Structural Mechanics Module. The RF module is based on Maxwell's equations of electromagnetic fields and waves, considered in Chapter 2. It provides advanced postprocessing features such as a far-field analysis. Application examples are antennas, waveguides and cavities, S-parameter analyses of antennas, and transmission lines. The structural mechanics module focuses on the structural deformation and stress analysis of components and subsystems and works in tandem with COMSOL Multiphysics [16].

FEKO is an electromagnetic analysis software using Method of Moment (MoM) with hybrid techniques employing FEM. Typical applications are antennas, antenna placement, RF components, radomes and so on. It is used in many industries such as automotive, aerospace, naval, RF components, antenna design, mobile phone, bio-electromagnetic, and even communication. There are three major components CADFEKO, EDITFEKO, and POSTFEKO about the FEKO user interface. CADFEKO is used to make geometry and do the required meshing for the FEKO solution kernel. EDITFEKO helps the user for creating or editing the input file. POSTFEKO is used for post processing purposes and visualizing the geometry of the FEKO model [17].

CST MICROWAVE STUDIO (CST MWS) specializes in 3D EM simulation of high frequency components such as antennas, filters, couplers and multi-layer structures. It provides six powerful solver modules: transient solver, frequency domain solver, eigenmode solver, resonant solver, integral equation solver and asymptotic solver. CST MWS uses a Finite Integration Method (FIM) and time domain analysis. In the time domain, the numerical effort of FIM increases more slowly with the problem size than other commonly employed methods [18].

HFSS is 3D full wave electromagnetic field simulation tool. It is one of the most well-known and powerful applications used for antenna design and the design of complex RF electronic circuit elements. It provides E-field and H-field, current, S-parameters, near and far field results. HFSS automatically creates a mesh for solving the problem using FEM. HFSS provides capability to analyze 3D radiating elements such as slot, horn, and patch antennas. It calculates, directivity, impedance, and radiation patterns [19].

Among its user groups, CST MWS enjoys a reputation as user-friendly software [20]. It provides both time domain and frequency domain analysis. In the case of FEKO, it can simulate efficiently large antennas such as used on aircraft and naval ships. Having large user groups, HFSS is perhaps the RF software best known over the world. COMSOL Multiphysics' strong point is that it can provide integrating solutions for multiple disciplines, such as electromagnetic and structures. In contrast to HFSS, CST, and FEKO, COMSOL Multiphysics has both structural

and EM analysis. Based on this feature among the choices surveyed, COMSOL was chosen for the initial SWASS design studies.

1.4 Problem Definition and Scope

A typical slotted waveguide model is shown in Figure 1.11. In Chapter 2, we shall first consider a multifunctional structure in which stiffeners act as slotted waveguides in Figure 1.12. To optimize these components, the design parameters such as geometric dimensions are defined in two categories. Firstly, one category is to optimize structures by minimizing weight, while achieving sufficient stiffness and strength to bear loads. In a structural optimization, the design variables are defined as the width, length, and thickness of waveguide antennas. The size of the waveguide structures obviously determines structural weight. In stiffness, the antenna shape influences the deformation of structures. The frequency of radiation determines the antenna size and the significant dimension of the slot. Secondly, antenna objective functions are specified in terms of desired gain, beamwidth of mainlobe or sidelobe, bandwidth, etc [13], governed by slot dimensions (Figure 1.10). In Chapter 3 we shall next consider design of waveguide tubes (Figure 1.11) that comprise the core of the sandwich structure of aircraft panels (Figure 1.12). Factors such as the dimension and location of waveguide slots are the EM design variables. To determine the value of design variables that optimize these functions for an approximate system response, a response surface method (RSM) [21] in ModelCenter was used in this research. Once derivatives are available, then more efficient multipoint approximations may be used [22].

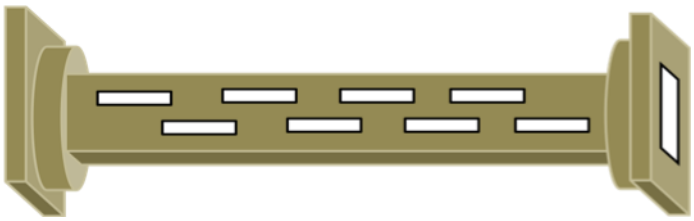

Figure 1.11. A simple slotted waveguide antenna

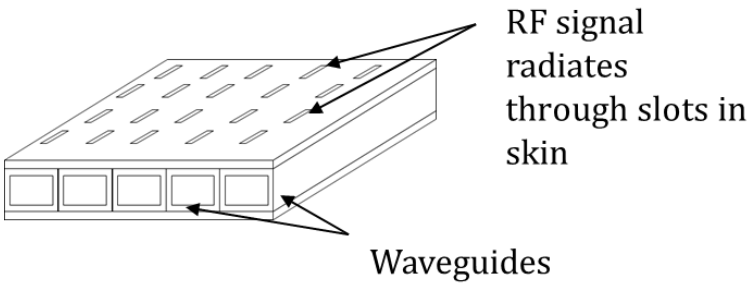

Figure 1.12. Stiffened waveguide structures

There are many materials for structures and antennas. Material properties affect the structural characteristics such as stiffness or strength and the antenna characteristics such as a gain or a beam pattern. In this research, composite materials are chosen for satisfying competing requirements of the structures and antennas. In addition, stiffener beam shapes, thickness or sizes are one of the important factors to support loads and radiate electronic waves. Therefore,

performance of the structures and antennas are varied by these factors. The factors can be used to optimize structural and antenna performance. These research goals are to search for the optimal structural and antenna design. To analyze the structure and antenna, a FEM is applied for both structural analysis and antennas for electromagnetic field analysis. The decoupled analyses were implemented in the SORCER [23, 24], as documented in Chapter 4, with a vision to eventually implement the coupled design via SORCER.

1.5 Summary of Research

Chapter 1 summarized a range of SWASS topic related to structural and electromagnetic design concepts and design variables for optimal conditions. Next, Chapter 2 presents a computational modeling methodology developed for design and optimization of slotted waveguide antenna stiffened structure (SWASS). A FEM-based model technique was used to configure a slotted waveguide array. Various geometric design variables were chosen for optimal design approach, which enables one to impose stringent conditions on structural configurations. Some of them are shown to have high impact on slot radiation pattern sensitivity. Sequential quadratic program (SQP) and response surface methodology (RSM) were used with the FEM-based modeling to quantify electromagnetic (EM) performance. Comparison of results from the two optimizers confirmed the extent to approximate optimal designs using RSM for the SWASS configuration which optimality conditions were satisfied

Chapter 3 addresses structural design and optimization of slotted waveguide antenna stiffened structures (SWASS). Structural design and optimization will be performed by designing the antenna structure imbedded aircraft panel subject to external loading, while evaluating radio frequency (RF) performance. For complex composite structural analysis, firstly, the equivalent model was proposed and compared to an analytical approach by simplifying 3D structure into 2D plate model. For higher fidelity, 3D plate FEM models for these structures were used to evaluate the mechanical failure and lightweight design criteria. This modeling technique is highly cost-effective in that it has relatively small number of elements compared with 3D solid modeling. This chapter demonstrated that it is sufficiently accurate compared to experiments and other published simulations.

Chapter 4 focuses on the development of the SORCER for the synthesis of mutiobjective function design and optimization through on-line database sharing. Structural analysis examples are demonstrated.

1.6 Deliverables

Various resources are saved at the websites “905123 Collaborative Center” and “SWASS” at scholar.vt.edu. The final report provides design models and analysis incorporating all journal/conference publications.

1.7 Technical Team Members

Technical Team Leader: Robert A. Canfield (PI), Professor, Dept. of Aerospace and Ocean Engineering Virginia Tech

Researchers: Woon Kim, Postdoctoral Research Associate,
Taekwang Ha, Graduate Student,
Garrett Hehn, Undergraduate Student,
Dept. of Aerospace and Ocean Engineering, Virginia Tech

Project Sponsor:
William Baron, Aerospace Systems Directorate, AFRL, WPAFB, OH
James Tuss, Aerospace Systems Directorate, AFRL, WPAFB, OH

Technical Support:
Jason Miller, Booz Allen Hamilton, Dayton, OH

Chapter 2 Radio Frequency Optimization of Slotted Waveguide Antenna Stiffened Structure

Woon Kim, Taekwang Ha and Robert A. Canfield
Dept. of Aerospace and Ocean Engineering, Virginia Tech, Blacksburg, VA, USA
William Baron and James Tuss
Air Force Research Laboratory, WPAFB, OH, USA
Keywords: SWASS, slotted waveguide, response surface methodology, radio frequency

2.1 Introduction

Traditionally, aircraft antennas have been designed independently from aircraft structures. These antennas are attached to an aircraft surface as blades or enclosed within the aircraft structure, typically covered by electromagnetically transparent and structurally weak composite materials such as fiberglass. In recent years, conformal load-bearing antenna structures (CLAS) have been considered to increase aircraft performance, such as the structural strength and stiffness, while maintaining the antenna Radio Frequency (RF) characteristics. The CLAS may be integrated into the honeycomb core, stiffeners or the skin of aircraft surface panel, so that the overall weight of structures can be reduced [2].

The slotted waveguide antenna stiffened structures (SWASS) belong to the CLAS concepts. It is a multidisciplinary blending of Radio Frequency (RF) slotted waveguide technology and stiffened composite structures technology and can be installed in the main part of load bearing structures. It will perform the roles of a structure and an antenna. [25]

Prior research on conformal load-bearing antenna structures (CLAS) has been dedicated to advance the technology of integrating structures and antennas to produce higher efficiency of the design and maintenance, since the need of multi-functional antenna design has emerged to increase safe and reliable aircraft performance [2]. The CLAS enables replacement of existing antennas with dual function of airframe panel structures that support primary structural loads and enhance EM performance along with weight saving.

Recent research has demonstrated that CLAS can provide RF antenna as well as stiffening structures. S^3TD was the first announced CLAS program managed by Air Force Research Laboratory (AFRL) from 1993 to 1996 [3]. Its goal was to verify that an aircraft antenna could be embedded in a structural part and bear actual load under operating conditions. An additional goal was to satisfy the antenna performance. S^3TD chose a multi-arm spiral antenna embedded in a body panel as its first test article. The multi-arm spiral was a wide field-of-view, broadband antenna element with unique properties that allowed it to perform threat location over its entire field-of-view. In the final demonstration, a 36 by 36 inch curved multifunctional antenna component panel was assessed. The panel bore 4,000 lbs/inch loads and principal strain levels of 4,700 microstrain. After 6,000 hours fatigue, one lifetime, the loads were applied to the panel to reach the ultimate. The ultimate load was 148 kips, which was one and half times the design limit load. In addition, they validated the wide band electrical performance for the panel, including avionics communication, navigation, and identification (CNI) and electronic warfare (EW) in the 0.15 to 2.2 GHz frequency range.

In 1997, the AFRL MUSTRAP program performed by Northrop Grumman Corporation started as a follow on to S^3TD [4]. The following two desirable concepts were investigated for MUSTRAP design. Firstly, the fuselage demonstration article was a load bearing multifunctional antenna in a 35 by 37 inch panel that supported an axial load of 1,800 pounds per inch and shear load of 600 pounds per inch. The load conditions replicated realistic flight load conditions.

Secondly, the vertical tail tip design concept is to avoid coinciding structural resonant frequency with RF. The new tail antenna performed comparably with the blade at its resonant frequency (~380 MHz), which is far away from the usable bandwidth either in the VHF-FM (30–88 MHz) or VHF-AM (108–156 MHz).

Smallwood *et al* [5] studied structurally integrated antennas on a joined-wing aircraft. They sought to embed conformal load-bearing antenna arrays into the wing structure of a joined-wing aircraft. Because the wings deform under the flight condition, it could affect the original configuration of the antenna. Therefore, the effect of wing deformation on antenna performance was simulated. A simple model of the sensors was generated to integrate the different layers of materials to construct the antenna's structure. A simplified finite element model consisted of five layers, which were an electromagnetically transparent material called astroquartz, two honeycomb core structures, and two graphite epoxy layers. Wing deformations were used to locate the new position and slope of each element of the array. Then, a new beam pattern was generated. Baseline results and repeated process results were compared to determine the beam pointing error due to the wing deformations for the various load configurations. He concluded that beam pointing error of about 9° was a maximum for a gust load.

One of innovative designs for CLAS is SWASS. The concept of SWASS is that conformal antennas are integrated into the honeycomb core, stiffeners or the skin of aircraft surface panels [26] . One of the primary concerns for SWASS is to ensure that the embedded waveguide antenna integrated with the composite structures resist external loads, and save weight but preserve antenna performance. Sabat and Palazotto [27] studied the nonlinear structural instability of a composite layer rectangular waveguide under uniaxial compression loads. Kim *et al* [28] proposed four novel design concepts of the multiple composite layer waveguides. The authors evaluated the mechanical failure and suggested lightweight design criteria.

In this chapter, computational methods are proposed to assess the EM performance with respect to geometric parameters of the waveguide such as the slot size, location and the cross-sectional dimension. The broad-wall waveguide was considered, where slots were cut through the top of the wall and aligned with the longitudinal direction. The finite element method (FEM) was used to investigate the overall response of radiation patterns. The FEM simulation results were employed in conjunction with the gradient-based and non-gradient based optimization techniques in order to quantify the geometric parameterizations.

2.2 RF Analysis of WR-90 Slotted Waveguide Antenna

2.2.1 Computational Modeling for Radiation

Figure 2.1 illustrates an end-fed WR-90 waveguide, operated in X-band frequency range, 8 to 12.6 GHz. One slotted waveguide is considered for EM analysis in the far-field region for two by two longitudinal slots were cut along the broad wall. It was assumed that the inside of waveguide is filled with air, and the waveguide surfaces are perfect electric conductors (PEC), excluding the slot region with a source at z = 0. Without another boundary on the z-axis, the wave propagates down the waveguide. As shown in Figure 2.1, the wave pattern consists of standing waves in the transverse directions (x and y) and a traveling wave in the longitudinal direction (z-axis). Since the side wall boundaries are perfectly conducting and the cross section is rectangular, the waveguide is dominated by the transverse electric (TE_{10}) mode [29]. For TE_{10}, the EM equations for the electric field and magnetic field components are given as [30]

$$
\begin{aligned}
E_x &= E_z = 0 \\
E_y &= -\frac{A_{10}}{\varepsilon}\frac{\pi}{a}\sin(\beta_x x)e^{-j\beta_z z} \\
H_x &= A_{10}\frac{\beta_z}{\omega\mu\varepsilon}\frac{\pi}{a}\sin(\beta_x x)e^{-j\beta_z z} \\
H_y &= 0 \\
H_z &= -j\frac{A_{10}}{\omega\mu\varepsilon}\left(\frac{\pi}{a}\right)^2\cos(\beta_x x)e^{-j\beta_z z}
\end{aligned}
\tag{2.1}
$$

with

$$
\begin{aligned}
\beta_x &= \pi / a \\
\beta_z &= \sqrt{k^2 - \beta_x^2} = \frac{2\pi}{\lambda_g} \\
k &= \frac{2\pi}{\lambda_0} = \frac{\omega}{c} \\
\lambda_c &= 2a
\end{aligned}
\tag{2.2}
$$

where λ_0 is the free space wavelength, λ_c is the cut-off wavelength and A_{10} is a constant at given (1,0) mode. The guided wavelength λ_g is defined as

$$
\lambda_g = \frac{1}{\sqrt{\left(\frac{1}{\lambda_0}\right)^2 - \left(\frac{1}{\lambda_c}\right)^2}}
\tag{2.3}
$$

The current density, $\mathbf{J}_s$, along the inner surface of walls are given

$$
\hat{n} \times \mathbf{H} = \mathbf{J}_s
\tag{2.4}
$$

where $\hat{n}$ is the unit normal vector to the surface. The current densities for the bottom wall surface are expressed as

$$
\begin{aligned}
J_x^{bot} &= -j\frac{A_{10}}{\omega\mu\varepsilon}\left(\frac{\pi}{a}\right)^2\cos(\beta_x x)e^{-j\beta_z z}, \quad for\ y = 0 \\
J_z^{bot} &= -A_{10}\frac{\beta_z}{\omega\mu\varepsilon}\frac{\pi}{a}\sin(\beta_x x)e^{-j\beta_z z}, \quad for\ y = 0
\end{aligned}
\tag{2.5}
$$

For top wall surface

$$
\begin{aligned}
J_x^{top} &= -J_x^{bot} = j\frac{A_{10}}{\omega\mu\varepsilon}\left(\frac{\pi}{a}\right)^2\cos(\beta_x x)e^{-j\beta_z z}, \quad at\ y = b \\
J_z^{top} &= -J_z^{bot} = A_{10}\frac{\beta_z}{\omega\mu\varepsilon}\frac{\pi}{a}\sin(\beta_x x)e^{-j\beta_z z}, \quad at\ y = b
\end{aligned}
\tag{2.6}
$$

The current density for left and right side walls are obtained as

$$J_y = j\frac{A_{10}}{\omega\mu}\left(\frac{\pi}{a}\right)^2 e^{-j\beta_z z}, \qquad at\ \ x = 0,\ a \tag{2.7}$$

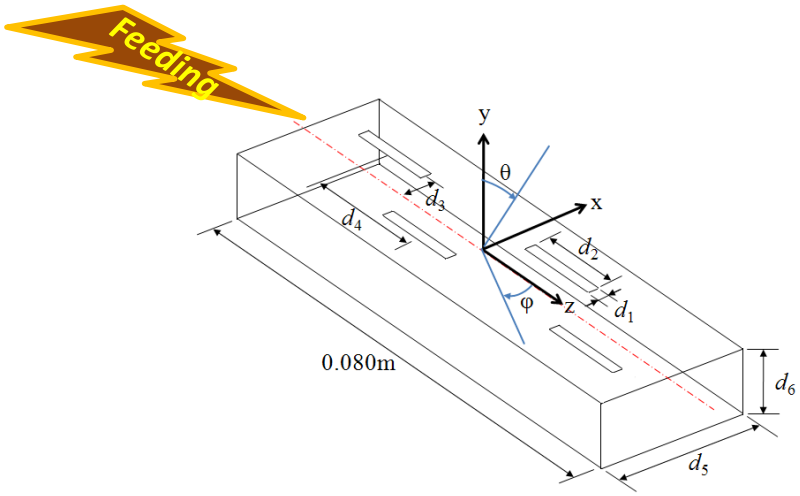

(a) Waveguide geometry and design variables

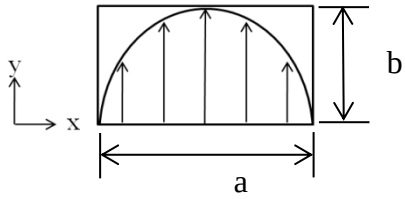

(b) TE_{10} mode of the waveguide

Figure 2.1. WR-90 rectangular waveguide antenna geometry

Six design variables were considered to investigate the E-field strength and sensitivity: d_1 is the slot width, d_2 is the slot length, d_3 is the distance from the waveguide center line in the x direction, d_4 is the spacing between slots, d_5 is the waveguide width, d_6 is the waveguide height and θ is the elevation angle measured from vertical and φ is the horizontal angle measured from z axis. The nominal six design variables were d_1 = 0.002m, d_2 = 0.010m, d_3 = 0.002m, d_4 = 0.020m, d_5 = 0.02286m, and d_6 = 0.01016m. For simulation, the waveguide was fed from one end at 10GHz with 1 W power. The electric field at the observation point($\mathbf{E}_p$) [16, 31]

$$\mathbf{E}_p = \sqrt{\lambda_0}\frac{jk_0}{4\pi}\mathbf{r}_0 \times \int[\hat{n}\times\mathbf{E} - \eta_0\mathbf{r}_0\times(\hat{n}\times\mathbf{H})]\exp(jk_0\mathbf{r}\cdot\mathbf{r}_0)dS \tag{2.8}$$

in which k_0 is the wave number of the free space, $\mathbf{r}_0$ is the unit vector pointing from origin to point p of the field, η_0 is the impedance of the free space, and $\mathbf{r}$ is the radius vector of the surface S.

2.2.2 Sensitivity results for WR-90 waveguide

In this section, the radiation patterns of the E-field in far field zone will be illustrated as a function of the elevation angle, θ, for a vertical plane passing through the longitudinal direction centerline of the waveguide, dot-lined in red in Figure 2.1. Figure 2.2 shows how slot dimensions influence the radiation magnitude. As the slot width d_1 approaches 0.003m, the far field magnitude in Figure 2.2(a) increases. Owing to the slot width, the difference between a maximum and minimum main lobe magnitude is about 3dB. Figure 2.2(b) shows that the slot length d_2 has an even stronger effect on the far field magnitude. The radiation magnitude increases as the slot length approaches 0.014m, which correspond to $\lambda_0/2$ at the operating

frequency 10 GHz. The difference between the minimum and maximum main lobe is almost 23dB.

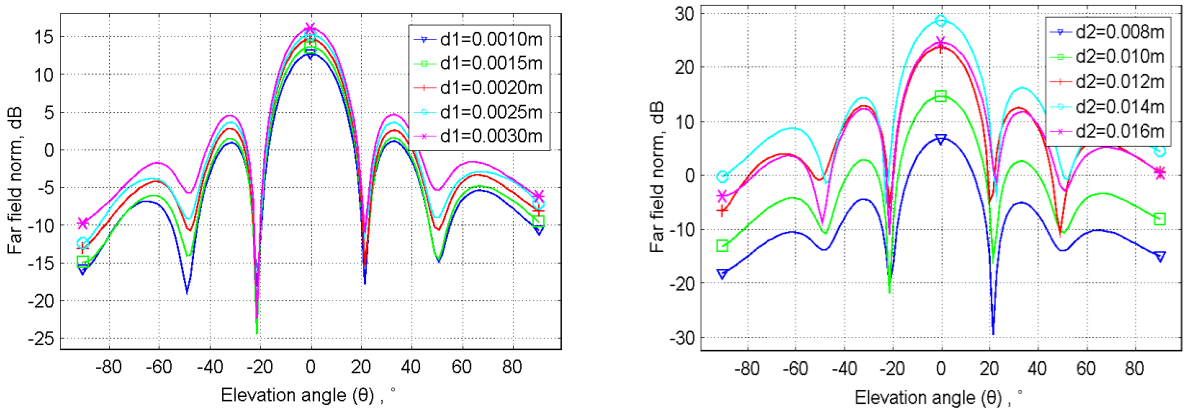

(a) Effect of slot width, d_1 (b) Effect of slot length, d_2

Figure 2.2. Radiation pattern of varying slot dimensions

Figure 2.3 shows how slot spacing on the wide wall of the waveguide affects the far field radiation magnitude. When the slot distance from the centerline is around 0.006m~0.010m in Figure 2.3(a), the beam strength is higher. Figure 2.3(b) shows that the greater the longitudinal spacing between two slots in the vicinity of the half guided wavelength ($\lambda_g/2$) which is 0.01985m calculated by Equation (2.3), the greater the magnitude.

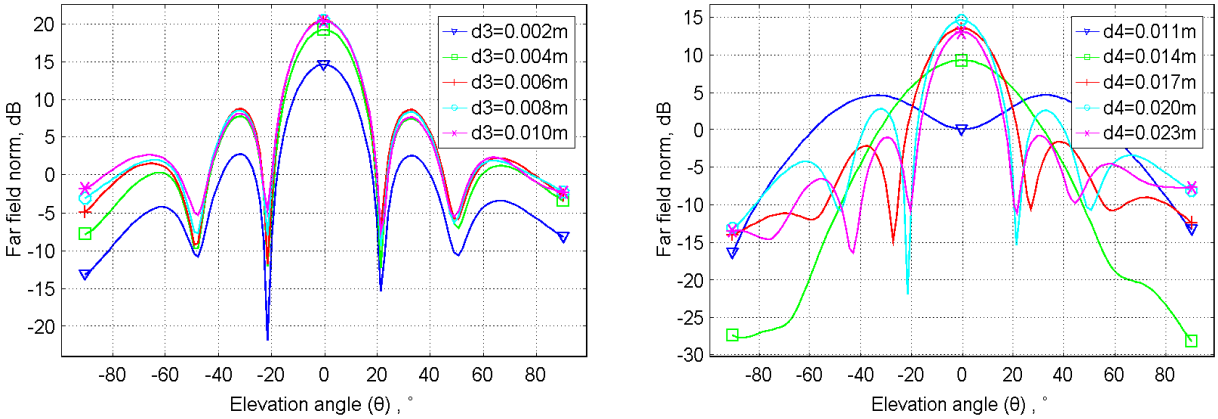

(a) Effect of slot spacing from the centerline, d_3 (b) Effect of longitudinal slot spacing, d_4

Figure 2.3. Radiation pattern of varying slot spacing

Figure 2.4 shows how the waveguide cross-sectional dimensions influence the radiation magnitude. The effect of the WR-90 waveguide width, d_5, is seen in Figure 2.4(a). Although the waveguide height in Figure 2.4(b) does not provide much change in the vicinity of the WR-90's height, 0.01016m, the smaller the waveguide height is than 0.01016m, the greater the magnitude.

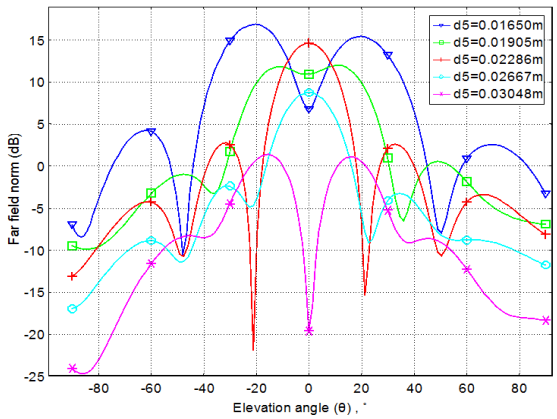

(a) Effect of waveguide width, d_5

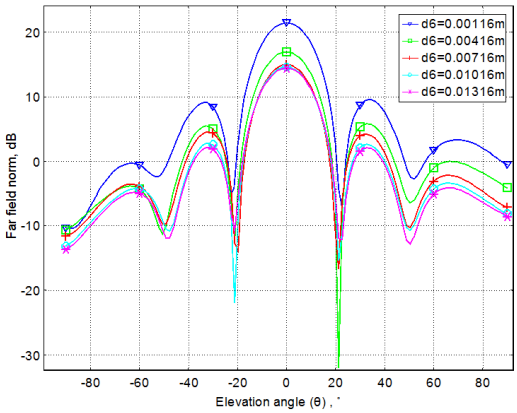

(b) Effect of waveguide height, d_6

Figure 2.4. Radiation pattern of varying cross sectional dimension of the waveguide

In order to visualize the main factors affecting to the response, the geometric variables were paired. The first three plots in Figure 2.5 are for pairs governing slot size, slot spacing and waveguide cross-sectional shape, respectively. Figure 2.5(a) shows that the slot width, d_1, has little sensitivity, while slot length, d_2, causes significant variation in the field strength. A local maximum with respect to slot length is apparent in this sub-space. Similarly, in Figure 2.5(b) peak magnitude has a large sensitivity with respect to slot spacing from the centerline, d_3, while little sensitivity is shown with respect to longitudinal slot spacing, d_4. Increased spacing from the centerline of the waveguide structure improves the far field peak magnitude, until the geometric constraints keep it from being increased any further. In contrast, although the longitudinal spacing has relatively little effect on the response, it does exhibit a local maximum on the interior of this interval. As can be seen in Figure 2.5(c), the waveguide width, d_5, is also a critical design variable to the antenna radiation. The waveguide height, d_6, on the other hand, does not have significant effect on the response. Again, a local maximum is apparent in this sub-space, this time with respect to waveguide width. Each one of these three response surfaces demonstrates high sensitivity with respect to one geometric variable and relatively little sensitivity with respect to the other paired variable in each response surface.

Having determined that the highly sensitivity variables are d_2, d_3 and d_5 from Figure 2.5(a) to Figure 2.5(c), it is worthwhile to examine the relationship between combinations of these high sensitivity variables, shown in Figure 2.5(d) through Figure 2.5(f). While response surface sensitivity with respect to the slot length is still high in Figure 2.5(d) and Figure 2.5(e), there is relatively low sensitivity with respect to simultaneous variation of the slot spacing from the centerline, d_3 and the waveguide width, d_5. Thus, there is little coupled interaction between these two variables, although d_2, d_3 and d_5 are sensitive variables individually. However, Figure 2.5(f) shows that the E-field peak magnitude for d_5 of 0.02m goes up with increasing slot distance from the centerline, d_3.

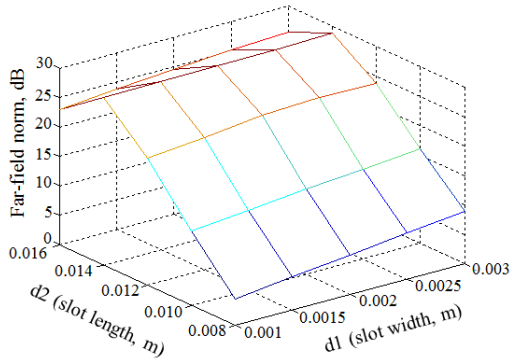

(a) Slot width (d_1) and slot length (d_2)

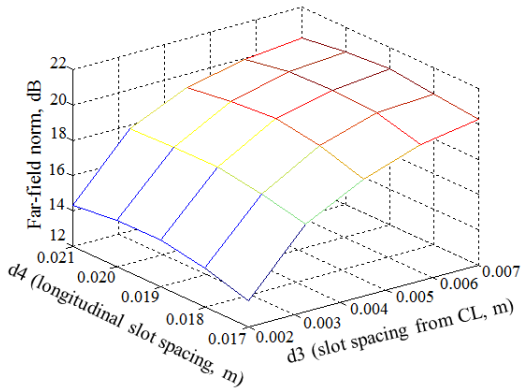

(b) Slot spacing from CL (d_3) and longitudinal (d_4)

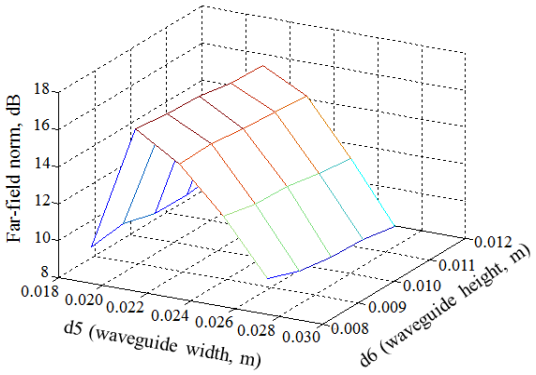

(c) WG cross-section (d_5 & d_6)

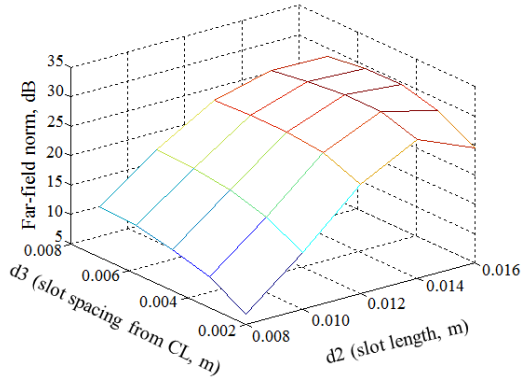

(d) Slot length(d_2) and slot spacing from CL(d_3)

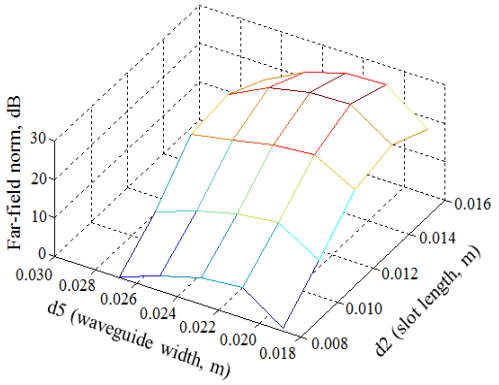

(e) Slot length (d_2) and WG width (d_5)

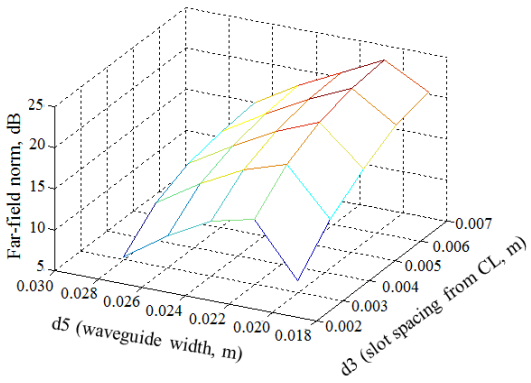

(f) Slot spacing from CL(d_3) and WG width(d_5)

Figure 2.5. Visualization of the effect of two factors affecting to the E-field Performance

2.3 Optimization

2.3.1 Problem Statement

In previous sensitivity modeling one-at-a-time and two-a-time variations were examined. Although each independent design variable had its own optimal size to improve RF performance with other variables fixed, simultaneous variation of all variables must be considered. During simultaneous optimization, appropriate relative constraints among the geometric variables must be enforced. In fact, combining the best independent values of geometric variables creates geometric inconsistencies, where four slots are positioned out of the structure as illustrated in Figure 2.6. Fixed side constraints have to be set to avoid this inconsistency, Equation (2.9). The objective function, $f(d)$, is minimized with respect to the design variables, d_1 to d_6, satisfying the geometric constraints . The minimized objective value is the negative of the magnitude of the E-field.

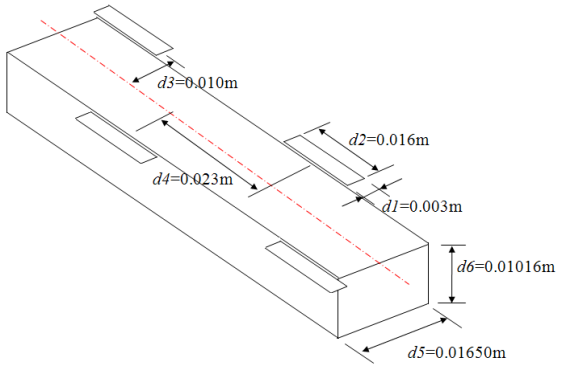

Figure 2.6. Geometric inconsistency

$$\min_{d} f(d) = -\left|E_p\right|^2$$

$$\text{Subject to} \begin{cases} 0.001m \le d1 \le 0.003m \\ 0.008m \le d2 \le 0.016m \\ 0.002m \le d3 \le 0.007m \\ 0.017m \le d4 \le 0.021m \\ 0.01886m \le d5 \le 0.02686m \\ 0.00838m \le d6 \le 0.01194m \end{cases} \tag{2.9}$$

2.3.2 Gradient-Based Optimization

a. Mesh Convergence and Step Size

Before a gradient-based optimization method was used for the RF optimal design with respect to all six geometric design variables, from d_1 to d_6, mesh convergence and step size studies were performed to assess the accuracy of the finite difference gradients. Step sizes varied as 10%, 5%, 1%, and 0.1% changes from the nominal values for each of six variables. Calculations using the following forward, backward, and central difference formulas, respectively, were compared.

$$f_f^{'} = \frac{f(x+\Delta x) - f(x)}{\Delta x} \tag{2.10}$$

$$f_b^{'} = \frac{f(x) - f(x-\Delta x)}{\Delta x} \tag{2.11}$$

$$f_c^{'} = \frac{f(x+\Delta x) - f(x-\Delta x)}{2\Delta x} \tag{2.12}$$

where $f_f^{'}$ is a forward difference (FD), $f_b^{'}$ is a backward difference (BD) and $f_c^{'}$ is a central difference (CD). For mesh convergence, meshes with nominal element sizes from maximum of 0.042m to minimum of 0.00056m meshes were created. As shown in Figure 2.7, as the mesh sizes become smaller, central difference derivatives are tending to converge for the finest meshes, where mesh1 is 0.0076m ~ 0.042m, mesh2 is 0.0056m ~ 0.0266m, mesh3 is 0.0039m ~ 0.021m, mesh4 is 0.0025m ~ 0.014m, mesh5 is 0.0014m ~ 0.0112m and mesh6 is 0.00056m ~ 0.0077m.

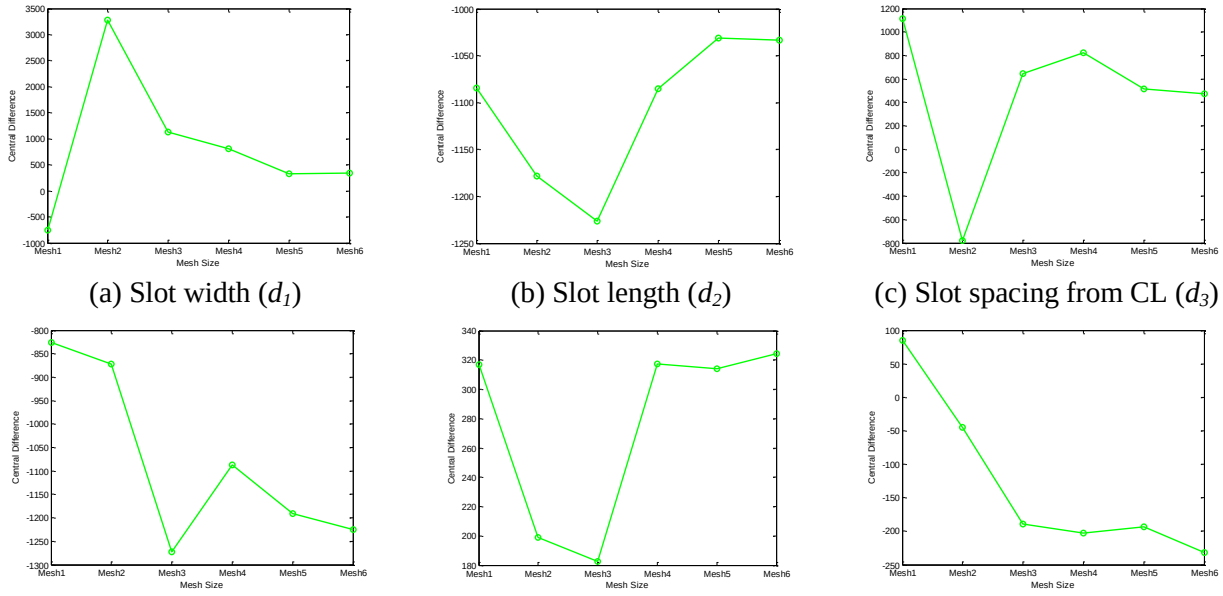

(a) Slot width (d_1) (b) Slot length (d_2) (c) Slot spacing from CL (d_3)

(d) Longitudinal slot spacing (d_4) (e) WG width (d_5) (f) WG height (d_6)

Figure 2.7. Mesh convergence for sensitivity. The vertical axis is central difference of E-field strength.

Figure 2.8 shows step size results with the various finite differences of E-field strength. The smallest step size consistently produces derivatives that diverge from the values found at larger step sizes. Depending upon the design variable, convergence appears to occur anywhere from 1% to 5% except for d_6, which does not appear converged. The reason that finite differences do not converge is that very small size variable difference such as 1e-10m varies the number of finite elements. Therefore, the finite differences did not converge monotonically. It is a good reason to apply larger step size or RSM. For gradient-based optimization, we applied the finite step size as 1e-3m for 0.0039m ~ 0.021m sized finite meshes.

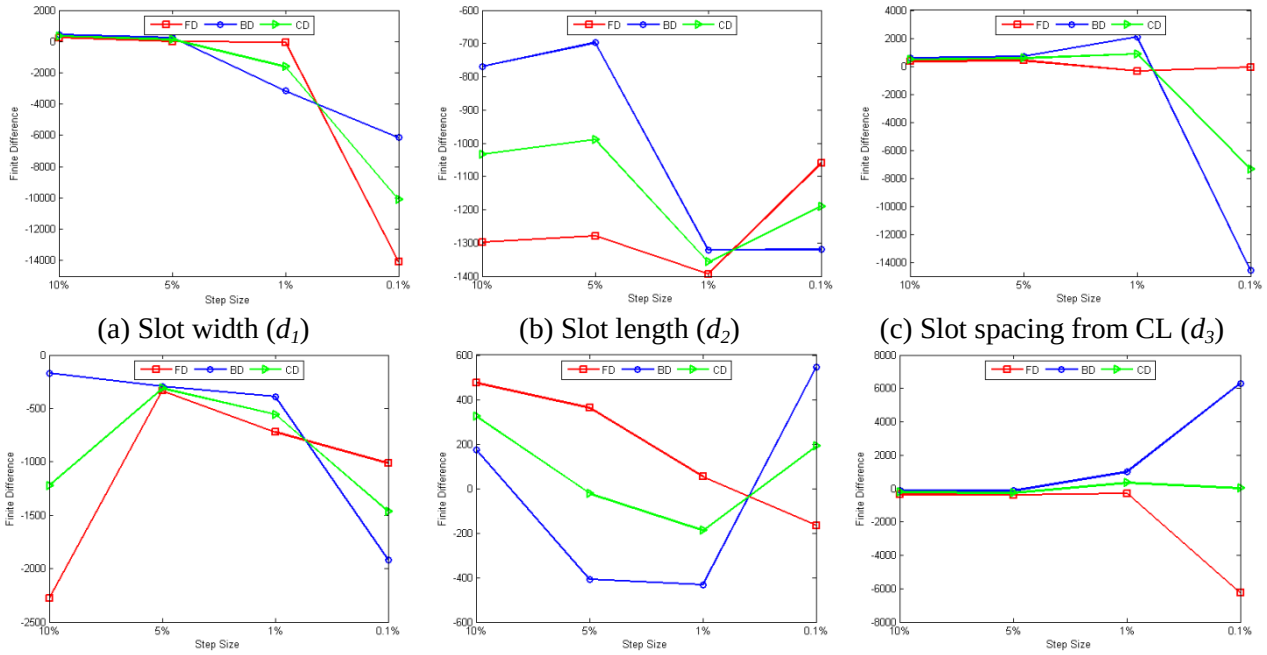

(a) Slot width (d_1) (b) Slot length (d_2) (c) Slot spacing from CL (d_3)

(d) Longitudinal slot spacing (d_4) (e) WG width (d_5) (f) WG height (d_6)

Figure 2.8. Finite difference of E-field strength with respect to step size

b. Gradient-based Optimization Results

Two commercial software products were used to investigate coupled geometric sensitivity for the gradients of RF performance. Sequential quadratic programming (SQP) algorithm [32] was interfaced with COMSOL Multiphysics via COMSOL LiveLink. ModelCenter [33] was also used to validate the optimization results. The starting values and optimized values are shown in Table 2.1. The step size for finite difference was set as 1e-3 in MATLAB. Figure 2.9 shows the comparison of radiation pattern between nominal values and optimal values. As shown in this figure, the E-field peak optimal value was double that at nominal value. It is seen that two optimal results computed from MATLAB and ModelCenter have a good agreement.

Table 2.1. Optimal Design Values

Design Variables	Nominal Values	Starting Values	COMSOL with MATLAB	ModelCenter
			Optimal Values	Optimal Values
d1	0.002m	0.002m	0.00226m	0.00300m
d2	0.010m	0.015m	0.01323m	0.01481m
d3	0.002m	0.004m	0.00349m	0.00379m
d4	0.020m	0.020m	0.01926m	0.01890m
d5	0.02286m	0.020m	0.02169m	0.02390m
d6	0.01016m	0.010m	0.00961m	0.00838m
E-field Peak Magnitude	14.7dB		30.2dB	30.4dB

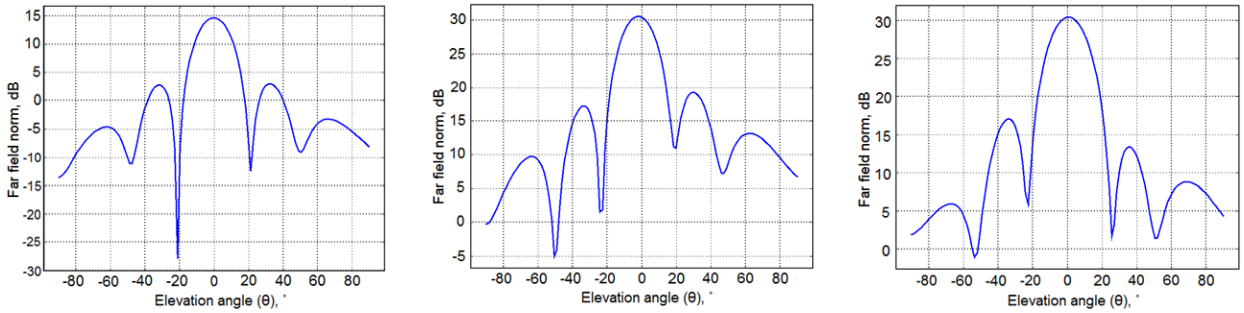

(a) Nominal values (b) COMSOL with MATLAB (c) ModelCenter

Figure 2.9. Radiation pattern of WR-90 Slotted Waveguide Antenna from Table 2.1

2.3.3 Response Surface Methodology

a. Design of Experiments

Design of Experiments (DOE) is a methodology to select location of design points at which sample the response of an engineered system [34]. DOE methods vary in their approach to specifying sufficient data for fitting a surface that will provide meaningful information in approximating the actual response. The DOE techniques examined for using RSM to design SWASS include Full Factorial Design (FFD), Central Composite Design (CCD), and Box-Behnken Design (BBD) [34] The number of design points required in each method is dictated by how many discrete values (or levels) are chosen for sampling each variable. One-level sampling chooses a single value for each variable. It is suitable for a choosing to approximate a response as a constant. Two-level sampling establishes two levels, a lower value and an upper value, for each variable. It is suitable for a linear response surface approximation or for averaging noisy sampled results for a constant approximation. Three-level sampling adds an intermediate value. It is suitable for a quadratic response surface approximation, or for more extensive averaging to fit a linear surface.

DOE methods differ in specifying what combinations of levels are used for the variables, also called factors. FFD requires sampling at every possible combination of regularly spaced levels among all the variables (factors). For example, the number of samples is eight (2^3) for two-level sampling of three factors as shown in Figure 2.10(a) and 27 (3^3) for three-level sampling of three factors as shown in Figure 2.10(b). Clearly, the weakness is that the number of samples increases dramatically as the levels and factors increase. BBD and CCD were created to combat this curse of dimensionality. Figure 2.10(c) shows that BBD samples a center point and points with extreme levels for two or three factors combined with midrange levels for the other factors. In CCD samples are selected from the center point of the design space plus the corner points and axial (or star) points for which factors are set to their midrange value except for one that is set to its outer (axial) values as shown in Figure 2.10(d).

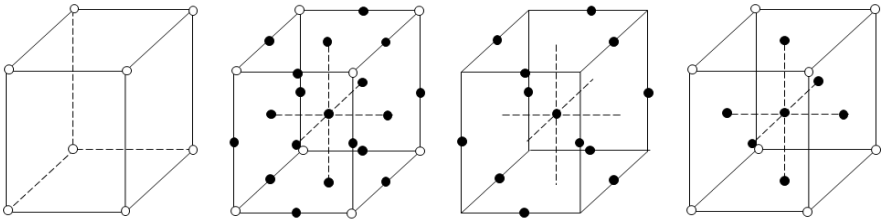

(a) 2-Level FFD *(b) 3-Level FFD* *(c) 3-Level BBD* *(d) 3-Level CCD*

Figure 2.10. Design of Experiments

b. Radiation peak results using RSM

RSM is a technique to approximate the response of a system by fitting sampled responses to a surface. The response surface approximation (RSA) may be used as a surrogate to evaluate the true response during a design optimization. Compared with gradient-based optimization acting upon the full-blown simulation, the RSA can approximate the response without the noise that decreases the quality of gradients used in gradient-based optimization. Although it is a good way to handle noisy data, sampling increases rapidly as the design variables increase.

Regression coefficients of second-order regression RSA model can be obtained from Least Squares Method as follows [35],

$$\hat{y} = \beta_0 + \sum_{i=1}^{k} \beta_i x_i + \sum_{i=1}^{k} \beta_{ii} x_i^2 + \sum \sum_{i<j}^{k} \beta_{ij} x_i x_j \tag{2.13}$$

This form can be expressed into vectors and matrices

$$\hat{\mathbf{y}} = \mathbf{X}\mathbf{b} \tag{2.14}$$

$$\mathbf{y} - \hat{\mathbf{y}} = \boldsymbol{\varepsilon} \tag{2.15}$$

$$L = \boldsymbol{\varepsilon}^T \boldsymbol{\varepsilon} = (\mathbf{y} - \hat{\mathbf{y}})^T (\mathbf{y} - \hat{\mathbf{y}}) \tag{2.16}$$

where $\mathbf{y}$ is the vector of exact solution obtained by sampling the true response model according to the chosen DOE technique, $\hat{\mathbf{y}}$ is the vector of an approximate solution, $\mathbf{X}$ is the matrix of the levels of the independent variables, $\boldsymbol{\varepsilon}$ is the vector of error, L is the least square function and $\mathbf{b}$ is the vector of the least square estimator.

The function is to be minimized with respect to $\boldsymbol{\beta}$. The least square estimator, $\mathbf{b} = [b_0, b_1, \cdots, b_k]$, must satisfy

$$\left. \frac{\partial L}{\partial \boldsymbol{\beta}} \right|_{\mathbf{b}} = -2\mathbf{X}^T\mathbf{Y} + 2\mathbf{X}^T\mathbf{X}\boldsymbol{\beta} = 0 \tag{2.17}$$

where $\boldsymbol{\beta} = [\beta_0, \beta_1, \cdots, \beta_k]$ is the vector of regression coefficients. Therefore, $\mathbf{b}$ can be expressed as

$$\mathbf{b} = (\mathbf{X}^T\mathbf{X})^{-1}\mathbf{X}^T\mathbf{Y} \tag{2.18}$$

Table 2.2 describes four response surface methods that were tested to compare their effectiveness by estimating and evaluating E-field peak magnitude in far field region. Two-level FFD required 64 simulations for the six factors in the current SWASS design, while three-level FFD required 729. In contrast, three-level BBD sampled 66 response simulations and CCD, 77. Linear (for level-2 FFD) or quadratic (for level-3) RSA for EM far-field peak magnitude were constructed by fitting these sampled data. Then they were used as surrogates in a numerical

optimization to maximize the approximate E-field peak magnitude in far field. The approximate E-field peak magnitudes by the optimization were compared with the actual magnitudes for the same design evaluated in COMSOL in the bottom row of the table.

As seen in Table 2.2, more levels for FFD coupled with the associated higher-order RSA provided better accuracy. However, higher level FFD to attain more accuracy comes at a price since the number of samples increased. In the BBD case, the reduced number of samples relative to FFD came at the expense of accuracy. However, CCD suffered much less in accuracy than BBD for a comparable number of samples, even though it reduced samples at the expense of accuracy. Therefore, the CCD will be a good choice SWASS EM design using RSM in that it produces a better peak magnitude than two-level FFD, three-level FFD and BBD. The CCD compared to three-level FFD has fewer samples: 77 times for CCD and 729 for FFD. It will still be significantly less costly than using 3-level FFD to improve accuracy, considering the fairly high computation cost in calculation. Obviously, the 2-level FFD RSA would not capture the curvature.

Table 2.2. Electric field peak magnitude using RSM

Design Variables		2-Level FFD	3-Level FFD	BBD	CCD
Number of Samples		64	729	66	77
d1		0.003m	0.003m	0.00256m	0.003m
d2		0.016m	0.01424m	0.01437m	0.01412m
d3		0.007m	0.00620m	0.00663m	0.007m
d4		0.017m	0.01882m	0.02m	0.017m
d5		0.01886m	0.024143m	0.01930m	0.02256m
d6		0.00838m	0.01194m	0.01m	0.00838m
E-field Peak Magnitude	ModelCenter	29.9dB	32.1dB	31.7dB	33.4dB
	COMSOL	25.5dB	29.5dB	26.7dB	29.0dB

Visualization of the CCD RSA with respect to pairs of variables is shown in Figure 2.11, which is similar to the visualizations plotted in Figure 2.5. The difference is that Figure 2.5 was created by sampling the six variables, d_1 to d_6, two at a time, with the other four variables held constant whereas the CCD RSA varies variables together and appears smoother, because it uses the second-order regression model in Equation (2.13). From Figure 2.11, d_2, d_3, and d_5 are still main effects for the E-field magnitude.

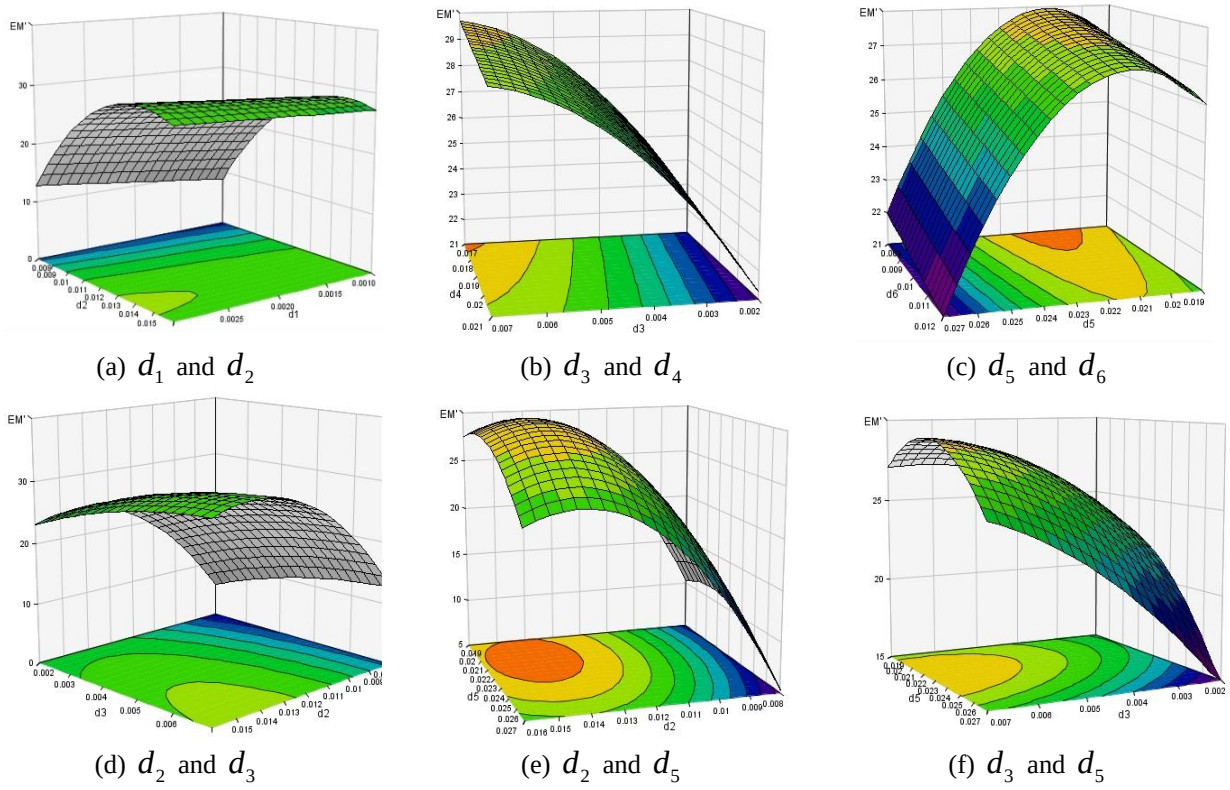

(a) d_1 and d_2 (b) d_3 and d_4 (c) d_5 and d_6

(d) d_2 and d_3 (e) d_2 and d_5 (f) d_3 and d_5

Figure 2.11. Response Surface Approximations from Central Composite Design (CCD)

2.4 Conclusions and Future Work

A computational modeling method for SWASS design optimization was proposed to investigate radiation pattern and its sensitivity. The variation in the structural geometry of the waveguide was quantified for EM analysis. Two-dimensional response surfaces of E-field strength illustrated that field strength was highly sensitive to three critical geometric variables; whereas it was weakly sensitive to the other three associated variables. In addition, the interactions among the strongly sensitive variables were weakly coupled.

Gradient-based (SQP) and nongradient-based (RSM) optimizers were compared. Both optimizers approximately doubled the E-field strength. Although RSM converged to 3dB higher radiation *approximate* value for its RSA than the gradient-based optimal value, the value computed by verification with COMSOL was slightly lower than the optimal value from SQP using central differences.

In the future, this research will be extended to formulate an integrated multidisciplinary design optimization (MDO) problem statement that incorporates the multiple objectives of minimizing structural mass and maximizing EM beam intensity, while satisfying structural constraints on strength and stiffness and EM constraints on EM beam pattern.

Chapter 3 Structural Design and Optimization of Slotted Waveguide Antenna Stiffened Structures Under Compression Load

Woon Kim and Robert A. Canfield
Dept. of Aerospace and Ocean Engineering, Virginia Tech, Blacksburg, VA, USA
William Baron and James Tuss
Air Force Research Laboratory, WPAFB, OH, USA
Jason Miller
Booz Allen Hamilton, Dayton, OH, USA

3.1 Introduction

Slotted waveguide antenna stiffened structures (SWASS) have been developed with the aim to improve the structural strength and stiffness of an integrated aircraft wing or fuselage, while evaluating electromagnetic (EM) or radio frequency (RF) performance. The essence of SWASS is basically to creating a Conformal Load-Bearing Antenna Structure (CLAS) by turning the skins of an aircraft structure into a radar system.

Figure 3.1 illustrates an example of an antenna-integrated structure. A major benefit is the weight savings. Conventional radar systems installed into an aircraft radome minimize aerodynamic loading effects; however, it is rather bulky and adds significant weight to the aircraft. Due to its honeycomb structure composition, the SWASS has the potential to lower the overall aircraft structural weight, while maintaining structural strength. Furthermore, SWASS utilizes the whole aircraft skin structure as a radar antenna which can significantly enhance the radar performance.

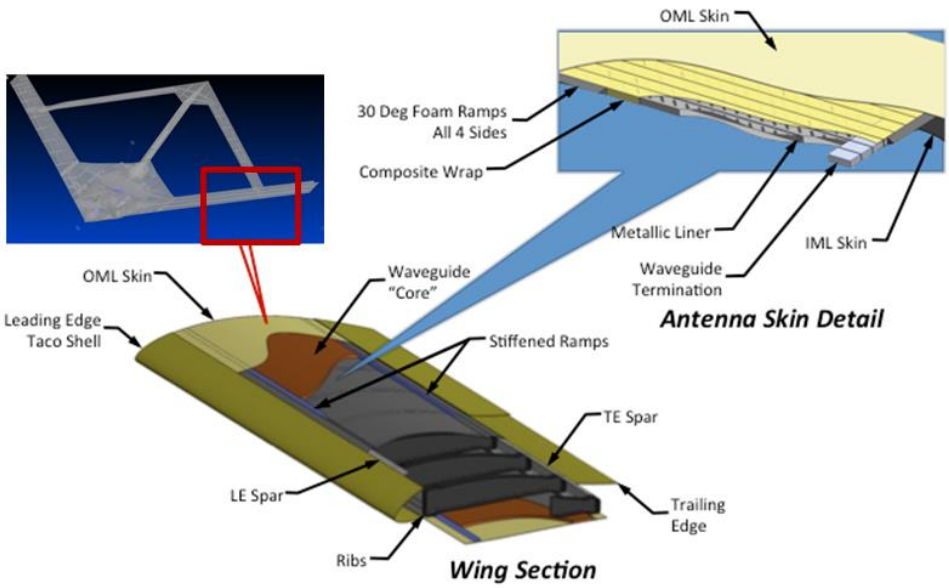

Figure 3.1. SWASS integration scheme

SWASS may be categorized as an advanced version of CLAS [2], which has received much attention due to its favorable characteristics, such as multi-functional integrity of aircraft and antenna structures. Callus [26] presented a brief history of the CLAS concept and reviewed various types of antenna-integrated structures.

The continuing work on SWASS has focused on improving structural performance by enhancing robustness and stability. Sabat *et al* [27] extensively studied structural failure and potential structural instability of SWASS through a single composite rectangular wave guide. Simulation results under uniaxial compressive load were verified against experiment results. Kim *et al* [28] presented modeling and analysis of four novel SWASS design concepts.

Kim *et al* [36] suggested an optimum design technique for WR-90 waveguide to maximize its EM performance. The authors investigated the trends of radio wave pattern sensitivity by varying the geometrical parameters of the waveguide. Regarding RF performance sensitivity associated with aircraft structure, Smallwood *et al* studied the dipole antenna-embedded structure on joined-wing aircraft [5]. The authors investigated the effect on sensitivity of RF performance due to structural deformation associated with aerodynamic loading. Knutsson *et al* tried to find or develop the materials not only to save weight, but also to increase electrical properties [37].

The SWASS design was formulated to minimize weight and maximize structural strength. This chapter presents three major things: (1) configuration of four design concepts of SWASS, (2) low-fidelity 2D and high fidelity 3D composite modeling and verification, and (3) nonlinear analysis for optimal design and experimental verification.

3.2 Design Concepts of SWASS

Structural analysis and evaluation of four novel design concepts for SWASS, shown in Figure 3.2, was carried out. These various composite structures possess a spectrum of performance capabilities characterized by 1) the stability subject to loading conditions, 2) effective mass ratio compared to the metallic reinforcement, and 3) the conductivities to be able to transmit an EM signal.

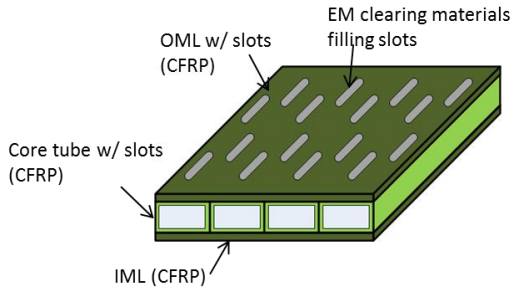

(a) Concept 1: Carbon tube with carbon skins

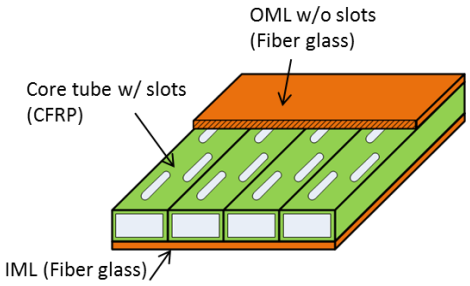

(b) Concept 2: Carbon tube with fiber glass skins

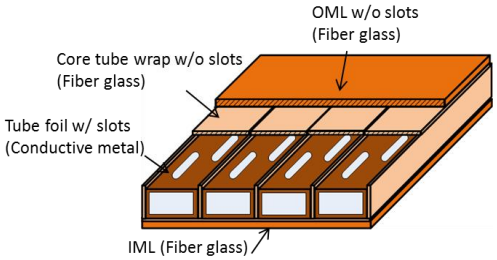

(c) Concept 3: Metallic foil WG: Foil wrapped by fiber glass with fiber glass skins

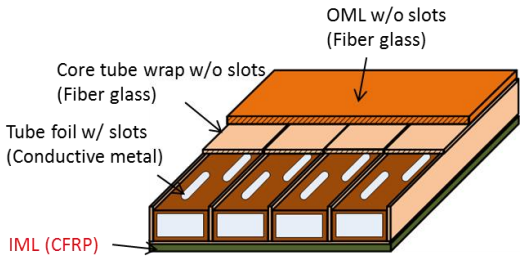

(d) Concept 4: Metallic foil WG: Foil wrapped by fiber glass with fiber glass (OML) and CFRP (IML) skins

Figure 3.2. Four design concepts of Slotted Waveguide Antenna Stiffened Structures

In detail, Concept 1 has load-bearing carbon fiber waveguide tubes enclosed by carbon-fiber inner and outer mold line face sheets. This structure is expected to effectively support various loads and as a result, prevent buckling and failure. In addition, due to conductivity of carbon fiber, EM signals can be guided by the fiber tube. Since the carbon fiber face sheets are also electrically conducting, slots must be cut through the top skins, which weaken structural stiffness. Concept 2 is similar to Concept 1, except that its face sheet material is fiberglass. Fiberglass is electromagnetically transparent, therefore no additional slots are required on the top skin, which is able to increase structural strength, even though fiberglass is not considered as stiff as carbon fiber.

Concept 3 is different from Concepts 1 and 2 in that it has thin copper metallic foil waveguide tubes to conduct electromagnetic signals. Only the metallic foil waveguide has slots, which has relatively less influence on mechanical strength. Face sheets are fiberglass, which is EM transparent; therefore no additional slots are required through outer skins. Concept 4 is same as Concept 3, except for replacing inner mold line (IML) material on the bottom face sheet with carbon fiber in order to increase stiffness. Figure 3.3 illustrates the detailed lay up of Air Force Research Laboratory (AFRL) SWASS test articles.

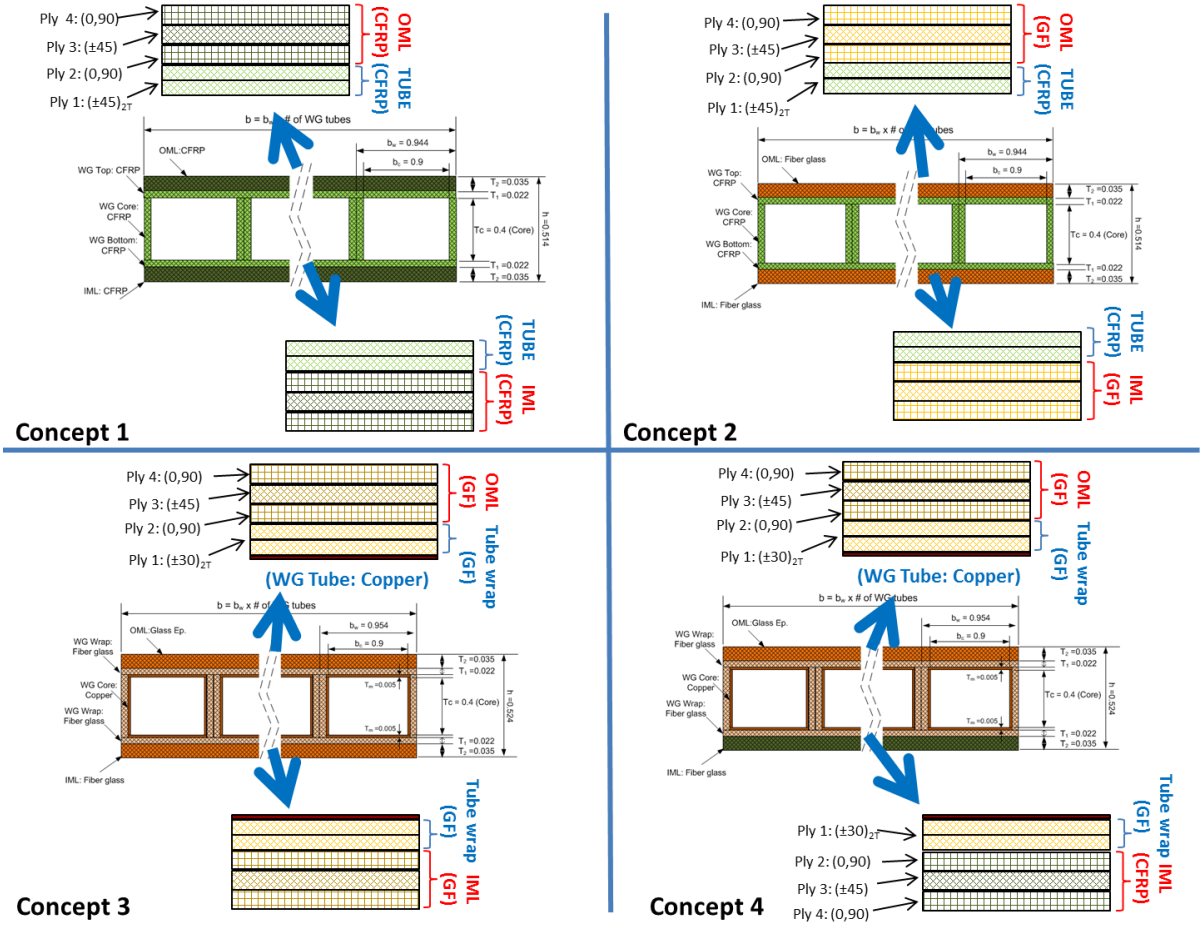

Figure 3.3. Layup configuration of four SWASS concepts

3.3 Equivalent 2D modeling

In this section, the mathematical derivation for 2D equivalent model is presented. It is analogous to a smeared honeycomb sandwich structure model in that the inherent material properties and geometries are reduced from 3D to 2D. The analytical approach follows the assumption of classical thin plate theory [38] including first-order shear deformation and is compared to 2D FEM model that may be more comparable to the analytical model.

3.3.1 Equivalent modeling of core webs

For model comparison and verification, two configurations of equivalent model are examined: firstly, equivalent core in Figure 3.4(a) and secondly, equivalent beam stiffness in Figure 3.4(b). The first configuration smears the web material across a homogenous core, while the second model the core web as beam stiffeners.

(a) Equivalent core

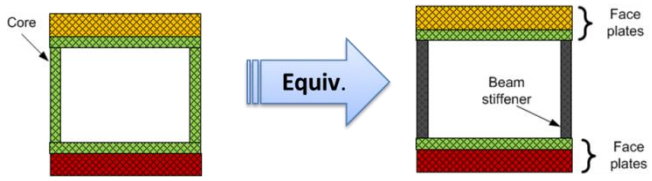

(b) Equivalent beam stiffness

Figure 3.4. Two configurations of equivalent model

The benefit of these approaches is to simplify the complex 3D composite structure for SWASS such as composite web columns in internal structure or slots on the surface plate into the corresponding 2D plate or 1D beam material problems. Another advantage is to save computational cost. Theoretical results demonstrate the accuracy and establish a guideline for suitability of an equivalent model.

3.3.2 Mathematical formation

The general expression for 2D equivalent plate model is derived from the principal virtual work problem [39, 40].

$$\delta U + \delta V = \delta \Pi = 0 \tag{3.1}$$

where $U + V = \Pi$ is the total potential energy, δU the virtual strain energy, δV the virtual work done applied forces. Specifically, the virtual strain energy (δU) is written as

$$\begin{aligned} \delta U = \int_V \Big[& \sigma_{xx}\delta\varepsilon_{xx} + \sigma_{yy}\delta\varepsilon_{yy} \\ & + 2\sigma_{yz}\delta\gamma_{yz} + 2\sigma_{xz}\delta\gamma_{xz} + 2\sigma_{xy}\delta\gamma_{xy} \Big] dV \end{aligned} \tag{3.2}$$

Classical laminate plate theory dictates that the strain components can be expressed as

$$\varepsilon_{xx} = \varepsilon_{xx}^0 + z\kappa_x,\ \varepsilon_{yy} = \varepsilon_{yy}^0 + z\kappa_y,\ \varepsilon_{yz} = \varepsilon_{yz}^0,$$
$$\varepsilon_{xz} = \varepsilon_{xz}^0,\ \varepsilon_{xy} = \varepsilon_{xy}^0 + z\kappa_{xy} \tag{3.3}$$

where plate curvatures κ_x, κ_y and κ_{xy} are given by

$$\kappa_x = -\frac{\partial \phi_x}{\partial x},\ \kappa_y = -\frac{\partial \phi_y}{\partial y},\ \kappa_{xy} = -\left(\frac{\partial \phi_x}{\partial y} + \frac{\partial \phi_y}{\partial x}\right) \tag{3.4}$$

For 2D modeling, the cross section of waveguide structures can be divided into three parts: top and bottom face sheets and web core in the middle. It is assumed that top and bottom skins support axial and bending/shear loads. And those can be easily modeled as thin plates. The web core improves structural responses by increasing stiffness. For simplicity, suppose that the web core mainly supports transverse shear and x-directional normal stresses. Hence, stress components distributed over the cross-sectional area can be expressed in terms of face sheets and equivalent web core. The stress-strain constitutive relation of laminate and web core for k^{th} layer is summarized as

$$\begin{Bmatrix} \sigma_{xx} \\ \sigma_{yy} \\ \sigma_{yz} \\ \sigma_{xz} \\ \sigma_{xy} \end{Bmatrix}_{(k)} = [\bar{Q}_{ij}]_{(k)}^{laminate+webequiv} \begin{Bmatrix} \varepsilon_{xx} \\ \varepsilon_{yy} \\ \varepsilon_{yz} \\ \varepsilon_{xz} \\ \varepsilon_{xy} \end{Bmatrix}_{(k)} \tag{3.5}$$

where $\bar{Q}_{ij}$ is an element of the transformed stiffness matrix aligned with the coordinate *x* and *y* axes.

The derivation of the constitutive relationship for stress and strain may be found in [40]. The rule of thumb is that each laminate skin is assumed to be in a state of plane stress, i.e., the normal stresses along z-direction are zero. The layers are assumed to be perfectly bonded together and linearly deform normal to the mid-plane. By substituting Equations (3.3) and (3.5) into Equation (3.2) in conjunction with the in-plane force and moment resultants, the in-plane stiffness matrix [A], the in-plane and out-of plane coupling stiffness [B], and the bending stiffness matrix [D] are expressed as

$$A_{ij} = \sum_{k=1}^{N_k} \left(\bar{Q}_{ij}\right)_k \left(z_k - z_{k-1}\right) + A_{ij,\ web\ equiv}$$
$$B_{ij} = \frac{1}{2}\sum_{k=1}^{N_k} \left(\bar{Q}_{ij}\right)_k \left(z_k^2 - z_{k-1}^2\right) + B_{ij,\ web\ equiv} \tag{3.6}$$
$$D_{ij} = \frac{1}{3}\sum_{k=1}^{N_k} \left(\bar{Q}_{ij}\right)_k \left(z_k^3 - z_{k-1}^3\right) + D_{ij,\ web\ equiv}$$
$$i, j = 1, 2 \text{ and } 6$$

where N_k is total number of laminate layers, z_k, z_{k-1} are the distance from the reference plane to the two surfaces of k^{th} layer. A set of equivalent web core stiffness matrices, $A_{ij,\ webequiv}$, $B_{ij,webequiv}$ and $D_{ij,\ webequiv}$, are calculated through the two methods. The details are shown in the following sections. For transverse shear stiffness matrix,

$$K_{ij} = \sum_{k=1}^{N} \left(\bar{Q}_{ij}\right)_k \left(z_k - z_{k-1}\right), \quad i, j = 4 \text{ and } 5 \tag{3.7}$$

The explicit expression for the transverse shear stiffness can be computed as strain energy balance under the assumption of the first-order deformation.

a. Equivalent core: Volume Fraction Approach

We assume that load is evenly distributed in the web core so that stiffness can be smeared across an equivalent single plate layer model. The equivalent material properties of Young's modulus (E^*) and shear modulus (G^*) can be expressed in terms of volume fraction (α)

$$\begin{aligned} E^* &= \alpha E, \quad \alpha = \frac{V_{ns} - V_s}{V_{ns}} \\ G^* &= \alpha G \end{aligned} \tag{3.8}$$

where E is the Young's modulus, G is the shear modulus, V_{ns} is the total volume of the internal core structure space, V_s is the total volume of web columns. Therefore, the three equivalent stiffness matrices, $A_{ij,webequiv}$, $B_{ij,webequiv}$ and $D_{ij,webequiv}$, are computed with single plate layer.

b. Equivalent beam

In the second model, the shear webs were modeled as beams to carry concentrated in-plane and shear loads. From Timoshenko-beam theory, the coupled governing equation is given by

$$\begin{aligned} &\frac{\partial}{\partial x}\left[\kappa^2 AG\left(\frac{\partial w}{\partial x} - \psi\right)\right] + p = 0 \\ &D\frac{\partial^2 \psi}{\partial x^2} + \kappa^2 AG\left(\frac{\partial}{\partial x} - \psi\right) = 0 \end{aligned} \tag{3.9}$$

where $w = w(x)$ is the transverse deflection, $\psi = \psi(x)$ is the bending slope, κ^2 is the shape factor, G is the shear modulus, $p = p(x)$ is externally applied force along the length of the beam, D is the bending stiffness. In this approach, the coupling matrix, $B_{ij,webequiv}$, is disregarded, since the neutral axis of beam stiffeners is set to the location of the neutral plane of the plates. Therefore, $A_{ij,webequiv}$ and $D_{ij,webequiv}$ are decoupled and modeled as beams.

3.3.3 Model verification

In order to verify the accuracy of the equivalent smeared stiffness approach, FEM modeling was performed in order to see the correlation with analytical approximation for Concept 1. Length, a, and width, b, are ten times greater than height, h for thin plate model. The NASTRAN-based FEMAP software [41] was used to model the composite layers with the equivalent core structures. The QUAD4 shell elements were used for the laminate skin plates [42]. The detailed material properties are shown in Table 3.1.

Figure 3.5 demonstrates the non-dimensional buckling load of the equivalent model along with theoretical results as a function of aspect ratio (a/b = length/width) under compressive uniaxial load with four simply supported edges. The two equivalent configurations, which are equivalent core and equivalent beam stiffeners, are well matched. However, there are differences between equivalent models and classical plate theory.

Table 3.1. Material properties [40]

	CFRP	Glass Fiber	Copper
E1($\times 10^6$ psi) (GPa)	20.1 (138.6)	7.8 (54.8)	18.0 (124.1)
E2($\times 10^6$ psi) (GPa)	1.2 (8.3)	2.6 (18.0)	18.0 (124.1)
G12($\times 10^6$ psi) (GPa)	0.6 (4.1)	1.3 (9.0)	6.72 (46.3)
G23($\times 10^6$ psi) (GPa)	0.72 (5.0)	0.5 (3.4)	6.72 (46.3)
G13($\times 10^6$ psi) GPa	0.72 (5.0)	1.3 (9.0)	6.72 (46.3)
υ_{12}	0.26	0.25	0.34
ρ (lb/in^3) (g/mm^3)	0.0659 (0.0018)	0.0686 (0.0019)	0.322 (0.0089)

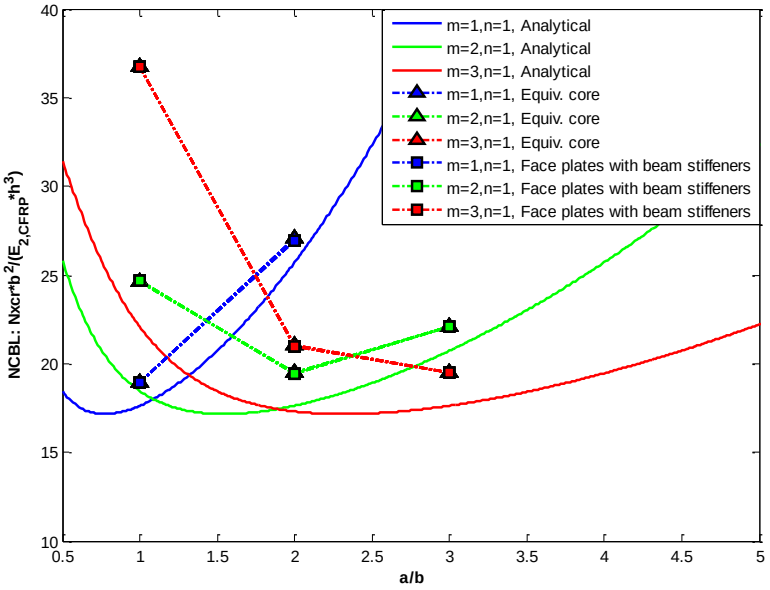

Figure 3.5. Comparison of volume fraction method and theoretical approach without slots

Figure 3.6 depicts trend of change of buckling load under consideration of slot size effect. The value of figure of merit of normalized buckling loads has been plotted as a function of Volume Fraction Factor (α). It is easily observed from both equivalent models that as the volume of slots increase, because of the reduction of equivalent stiffness, the nominal buckling loads decreases. However, there are significant differences between equivalent model and slots modeled in the mesh (FEM) at α=0.9. Clearly, there is still considerable approximation involved in this approach for structural evaluation and verification with three-dimensional approach, which generally has higher fidelity.

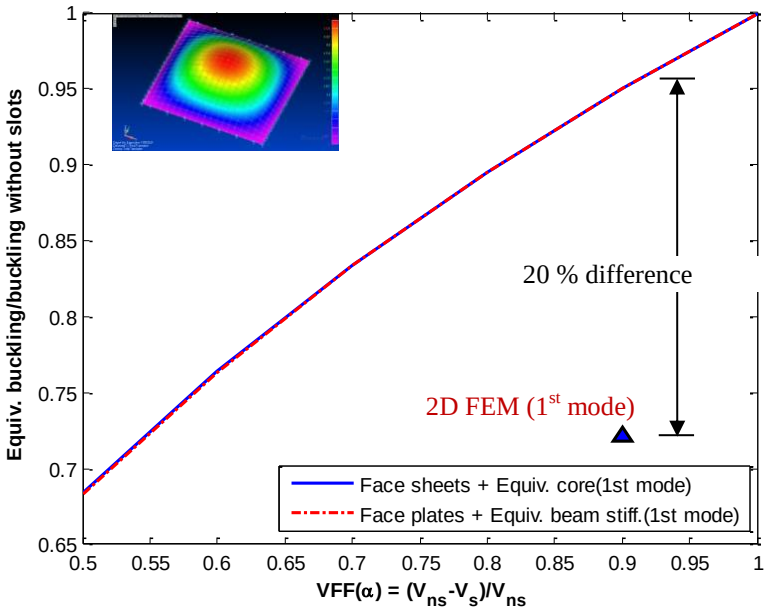

Figure 3.6. Slot volume fraction effect: four simply supported edges under uniaxial compressive load

3.4 3D FEM Plate Model

The buckling response of a 3D plate model was evaluated through comparison with a previous model studied by Sabat *et al* [27] and extended to the application of the four SWASS design concepts.

3.4.1 Model verification of 3D plate FEM model

It is worthy to investigate our proposed 3D plate model by comparing with previous work that simulates a single rectangular tube CFRP composite structure [27].

Table 3.2 shows the simulation result of the critical buckling load for non-slotted and slotted waveguide tubes. As can be seen from the table, the difference of simulation results of buckling between Sabat's and 3D plate models is less than 3%. The 3D plate model matched Sabat's 3D solid model well, whereas the 3D plate model has significantly fewer number of elements than Sabat's solid model. The important conclusion to draw from the table is that the 3D plate model is more efficient than Sabat's model, since it saves computation cost and is relatively accurate. However, neither simulation results match experimental results well. Further investigation is required to explain the discrepancy.

Table 3.2. Comparison of structural instability between Sabat's and 3D plate models

	Exp. [27]	Sabat [27]	3D plate
Non-slotted (1st mode)	730.0	938.7 (28.6%)	928.9 (27.4%)
Slotted (1st mode)	640.0	863.3 (35%)	892.2 (39.4%)
# of Elements	N/A	40,000 (Approx.)	1,000 (Approx.)

Difference in parentheses ( ) is between FEM and experiment: |FEM – Exp.|/Exp × 100 (%)

3.4.2 Structural instability of four design concepts of SWASS

AFRL recently provided four novel design concepts of SWASS for parameterization with varying panel dimensions and boundary conditions for prediction of buckling and failure. The coordinate and loading conditions for three-tube sticks are illustrated in Figure 3.7.

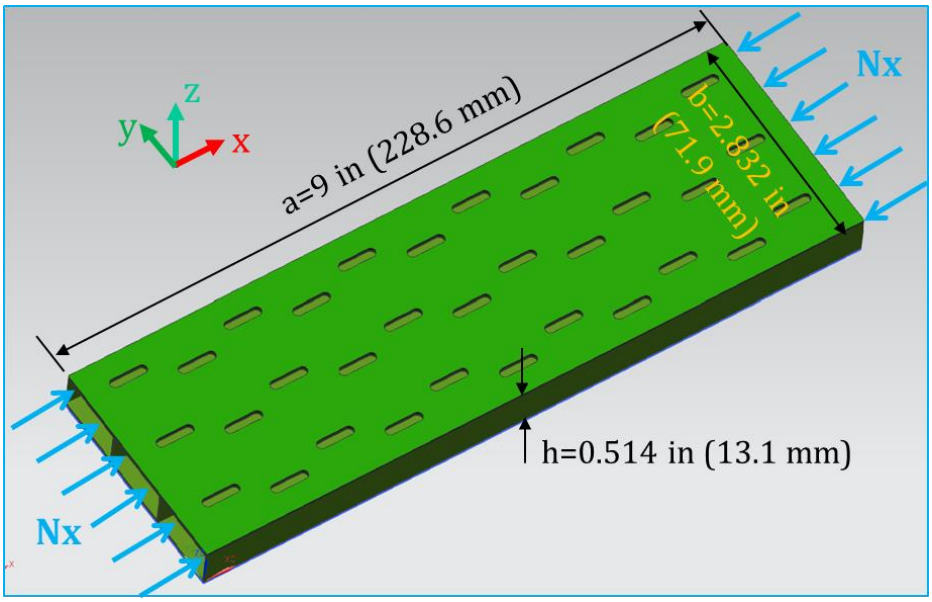

Figure 3.7. Configuration of three waveguide tubes in SWASS sandwich construction panel under uniaxial loading

Contour plots of buckling mode shape deformation are shown in Figure 3.8. The transverse deflection pattern of the SS case looks like Euler beam-column behavior: a half sinusoid wave as shown Figure 3.8(a). However, another pattern of the deflections of the CC are illustrated in Figure 3.8 (b). Many sinusoidal waves are seen in top face sheet layers (we call it a local mode) that are structurally weakened by slots. One interesting result is shown in Figure 3.8(c) where local buckling was found at the bottom panel in concept 4, rather than on top, even though top face sheet layers are considered to be softer stiffness. This indicates that bottom face sheet layers carry more load when the uniaxial load is applied, and resulted in their buckling first.

Figure 3.9 shows the buckling comparison of a 3D plate model for the waveguide structures. These are three-tube slotted waveguides with simply supported (SS) and clamped-clamped (CC) boundary conditions on both ends, under distributed uniaxial load on the cross-section of the waveguide tube. Critical buckling is normalized by the 1st global buckling of concept 1 with the SS boundary condition. The SS boundary condition on both ends may not be realistic, but is useful as a lower bound for a more conservative buckling load than the CC boundary condition on both ends. The local buckling loads are approximately 1.5 times higher when slotted waveguides are designed with thin metallic foil tube with fiber skins (concept 3 and concept 4). Concepts 1 and 2, which have a carbon fiber tube with composite laminate skins, in contrast, have a low critical buckling load.

Another plot of the non-dimensional, uniaxial buckling load normalized by weight for the four waveguide concepts is shown in Figure 3.10. On the vertical axis, the weight-normalized buckling load is plotted where normalized buckling factor is divided by the weight of concept 1. Three curves are shown, corresponding to the normalized buckling factors in Figure 3.9. Most

importantly, this figure provides insight into buckling variation over mass ratio and provides a lightweight design criterion. In local buckling, the thin metallic foil composite waveguides have high stiffness, as well as weight efficiency, even though they are composed of metal foil having high mass density. For global buckling, concept 1 has good weight efficiency, since it is a composite structure and the lightest of all four concepts.

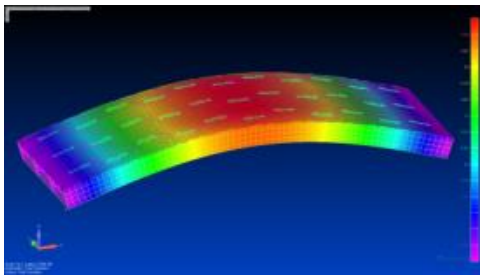

(a) Concept 2, SS, global mode

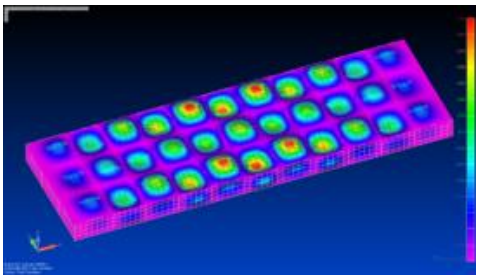

(b) Concept 3, CC, local mode

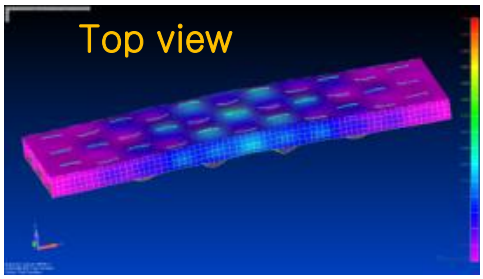

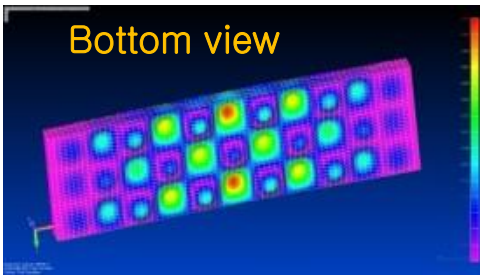

(c) Concept 4, CC, local mode

Figure 3.8. Contour of buckling mode shapes

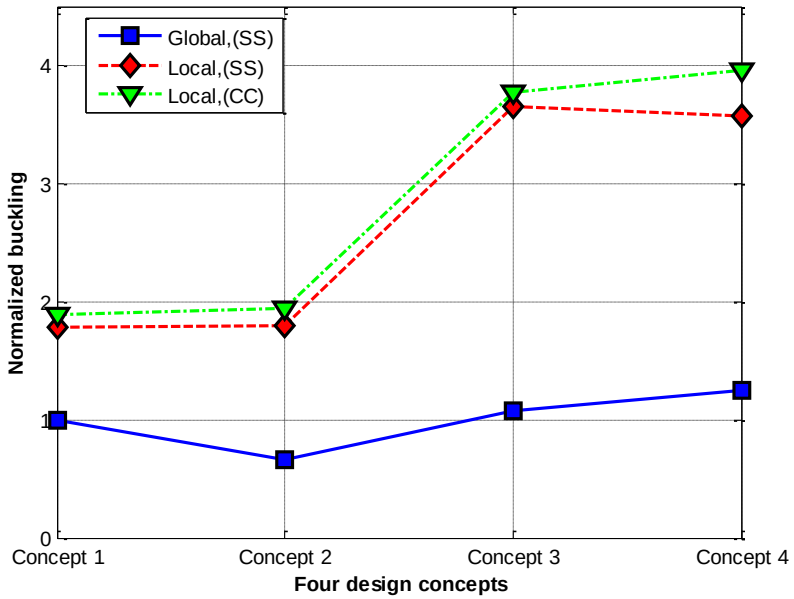

Figure 3.9. Buckling response of three-tube slotted waveguides, where normalized buckling factor is buckling load/(1st global buckling load (SS) at concept1)

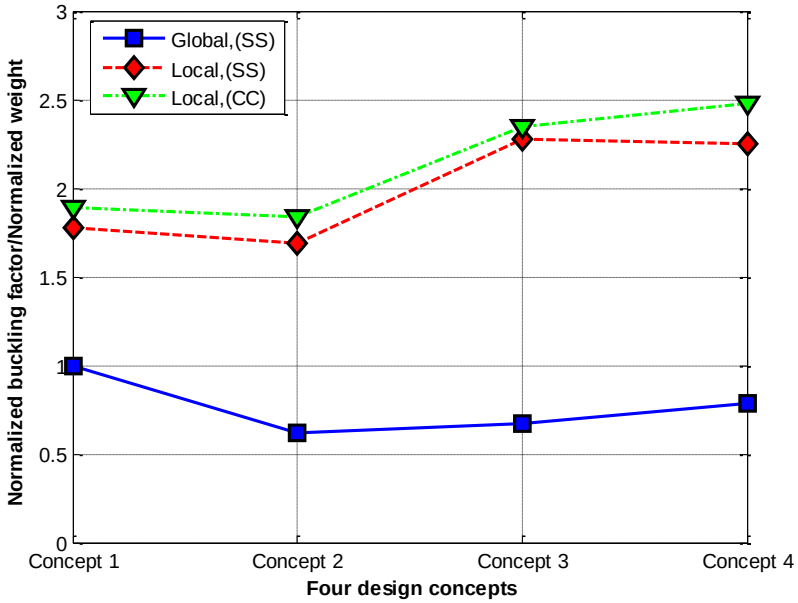

Figure 3.10. Weight-normalized buckling of three-tube slotted waveguides, where Normalized BF = Buckling load/(1st global buckling load (SS) at concept1), and Normalized Weight = Weight at each concept/(Weight at concept1).

3.5 Structural Analysis and Evaluation

3.5.1 Nonlinear analysis

Three waveguide tubes in a SWASS sandwich construction panel with composite face sheets were modeled for FEM nonlinear analysis [41, 42]. For the analysis a variety of boundary conditions were considered. Figure 3.11(a) shows fully clamped boundary condition (fully CC) on both ends where all six degrees of freedom are fixed. As shown in the figure, end corners are highly strained (or stressed) with this boundary condition, which makes the analysis rather conservative. For practical design, these zones should be mitigated. Loosely clamped BC (loosely CC), shown in Figure 3.11(b), is less strictly clamped BC since the wide (y-axis) and transverse (z-axis) directions are mostly free, so that the concentrated stress or strain zones go away from edges or corners. Loosely clamped ends eliminated local end effects from driving the design.

Figure 3.12 shows strain in fiber directions as a function of the compressive load for the four SWASS design concepts. Strains from the FEM model were obtained at the outer layer surface where maximum strains in the fibers are expected. The dashed vertical lines in the figure represent the ultimate strain limits. AFRL provided the allowable fiber strain criterion of 4000 μ-strain. For the applied design load, Concept 4 is considered in more detail, since buckling analysis in previous work [28] showed that Concept 4 had the highest structural resistance when the metallic waveguide supported loads (load-bearing waveguide). The transverse deflection curve (pink-dotted line) in Figure 3.12(d) indicates the fiber strain in the region of maximum transverse deflection, which is associated with the path for buckling. Through nonlinear load-deflection analysis, the fiber strain reached the allowable strain prior to (local) buckling. That is, the allowable strain constraints prevent buckling from becoming critical. The strain limit

corresponds to 12,000 lb_f (53.4kN) compressive load—the maximum design load used for optimization.

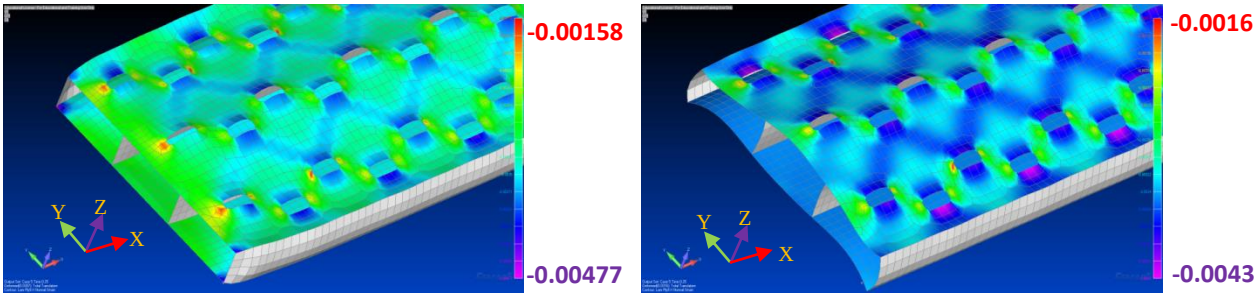

(a) Fully clamped (b) Loosely clamped

Figure 3.11. Two different boundary conditions: contours on top and bottom face sheet strains in fiber direction (concept 1). Unit: in/in

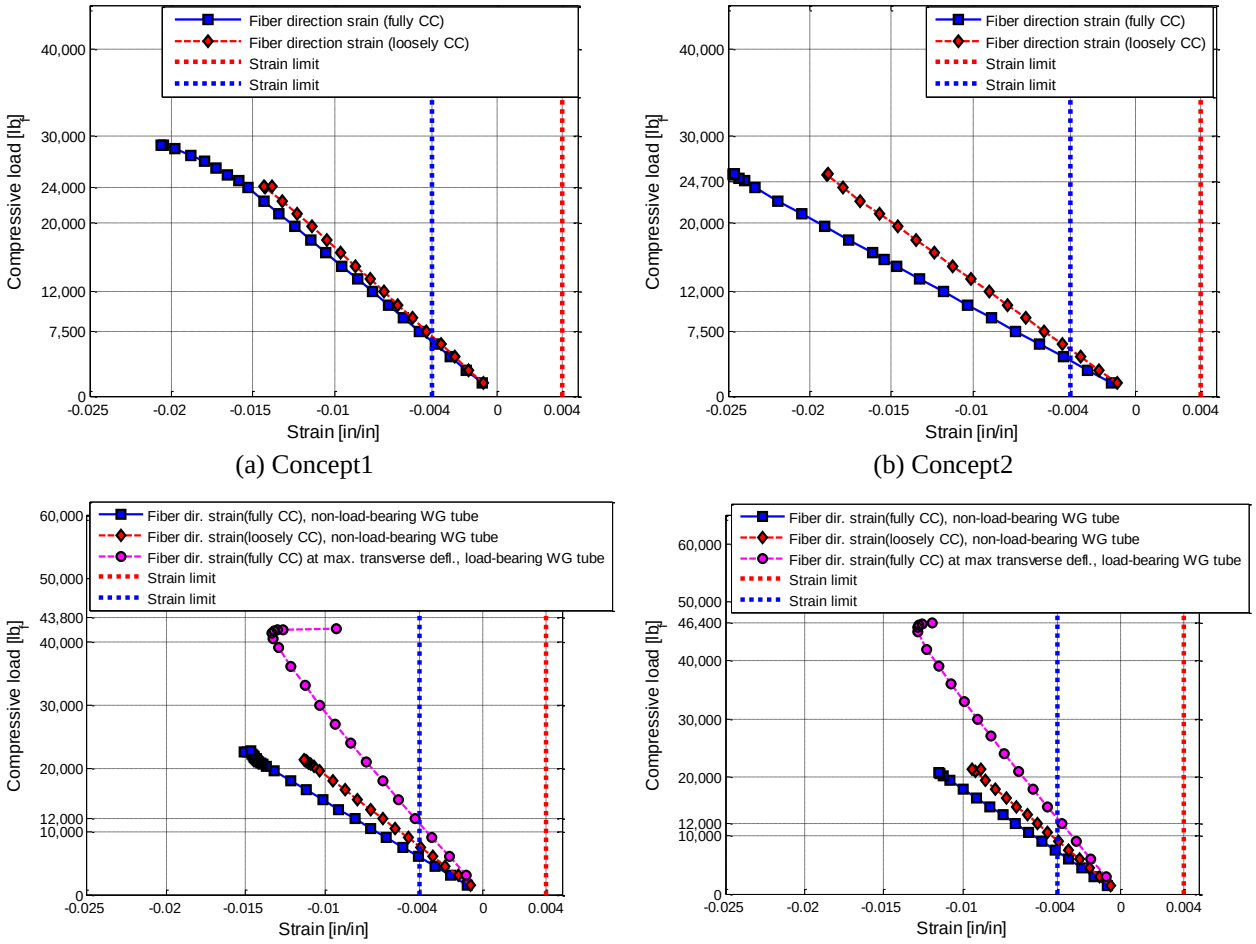

(a) Concept1 (b) Concept2

(c) Concept 3 (d) Concept 4

Figure 3.12. Fiber direction strain under compressive loading in the initial design. The applied design load (12000 lbf (53.4kN)) is determined by the circular pink-dotted line of Concept 4 (1000 lb_f = 4.45kN)

3.5.2 Structural optimization

In SWASS structural optimization, weight reduction is critical, while achieving sufficient stiffness and strength to bear loads. The failure criteria considered is the design strain limit and the critical buckling mode as determined through the nonlinear analysis as shown in the previous section.

$$\begin{cases} \min\limits_{d_S} \; W = f(d_S) \\ s.t. \;\; \text{design strain limit: } \varepsilon_f \le \varepsilon_{f,allow} = 4000\,\mu\varepsilon \\ \qquad \text{applied design load: } P_{cr} \le P_x = 12000 lb_f \end{cases} \tag{3.10}$$

where W is the weight, d_S is the structural design variables. NASTRAN optimizer was used with composite layer thickness design variables.

Figure 3.13 summarizes the weight change of the four SWASS design concepts before and after optimization. Among the initial designs, Concept 1 was the lightest composite structure, because of the lowest mass density of carbon fiber, whereas, due to the copper metallic foil, Concepts 3 and 4 were the heaviest. The pink and red dotted lines represent post-optimization curves with different boundary conditions. The red dotted line corresponds to the fully CC on both ends and the pink dotted line, loosely CC. They affect post optimization weight, since the highly concentrated load at the corners of the fully CC makes layer thicknesses increase more than the loosely CC after optimization.

Concepts 1 and 2 increased the overall composite layer thicknesses in order to satisfy the ultimate strain design criterion after optimization, resulting in a weight increase. Due to the large structural stiffening of CFRP, Concept 1 had small weight variation, compared to Concept 2. There are two reasons for the highest weight increase rate (or laminate thickness increase rate) in Concept 2 among the four concepts. First, the glass fiber layers in the top and bottom skins weaken the stiffness more than the CFRP does in Concept 1. Second, the layer orientation of the waveguide tube in Concept 2 is ±45°, versus ±30° (waveguide wrapping) in Concepts 3 and 4. Load was distributed more over the top and bottom face sheets. Therefore, the strain becomes larger there, leading to the large thickness variation to prevent strain failure.

For Concepts 3 and 4, it was assumed in the initial structural analysis that the metallic waveguide foil carried load. However, for an optimal design, it was assumed that the metallic foil will not be adhered to the skin and therefore does not carry loads, in order to avoid degrading antenna performance from foil deflection. Thus, Concept 3 increased the weight, since the composite material carries the entire load, even though the strain limit at the applied design load is almost the same as the ultimate strain design limit at the initial design. Concept 4 has little weight variation relative to Concept 3, because the bottom skin structure (carbon fiber) has higher stiffness than the top skin (fiber glass). Therefore it carries load more efficiently, becoming thicker, compensating for the relatively thinner top skin.

Figure 3.14 illustrates the nonlinear load-strain responses after optimization, which meets the strain and load design criteria. Concepts 1 and 4 have not only consistent resistance to load and strain, but also little variation of mass. This implies that glass fiber-based structures may be screened and CFRP-based or mixed structures with CFRP can be used.

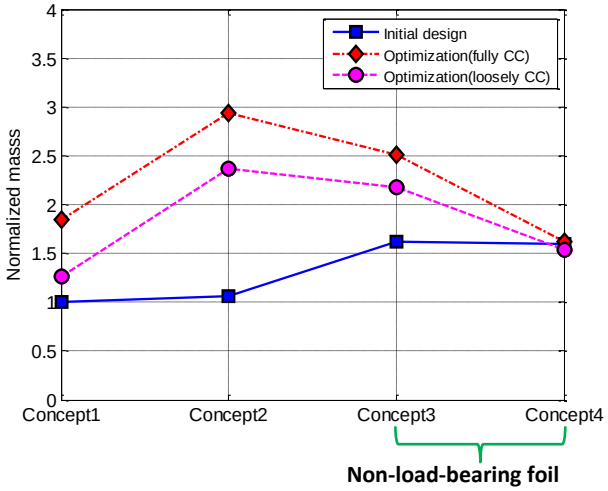

Figure 3.13. Mass efficiency for four different SWASS design concepts before and after optimization

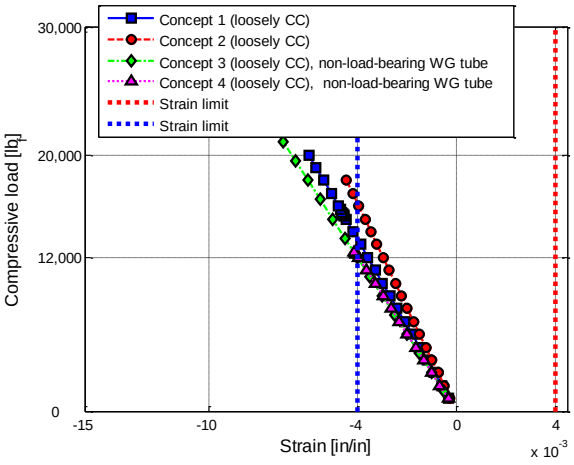

Figure 3.14. Post-optimization curves.

3.5.3 Experimental results

The specimens corresponding to Concepts 3 and 4 were chosen for comparison with tests. Concept 4 specimens use Fibreglast style 7718 glass fiber weave for top skin, Fibreglast style 660 carbon weave for bottom skin. The 0.005-inch (0.127 mm)-thick waveguide tube is wrapped by Fibreglast 2610 glass biaxial glass fiber. Bottom skin of Concept 3 specimens use Fibreglast style 7718 glass fiber weave. The overall sizes and lay-up orientations are shown in Table 3.3. For simulations, we assumed that composites are perfectly bonded, and woven fabrics are stacked layer by layer. The general material properties were used as shown in Table 3.1, since the manufacturer does not provide material properties.

The compressive load test was done using the MTS machine test as shown in Figure 3.15. Test device and fixtures follow ASTM C364 to measure load-bearing capacity. Strain gages were placed at center point of outer surface on both sides for the data collection in the longitudinal direction, that is, compressive loading direction. Results for two sets of boundary conditions are shown: clamped and simply-supported conditions on both ends. The silver cylinder clamped the test panels, so the panels cannot experience rotations and deflections at both ends. The silver cylinder and black jig line contacted. Therefore, it allows the panels to rotate about the cylinder center axis, although there is friction. For simulation, we considered two extreme cases, SS and clamped respectively, because these two simple conditions should bound the results for the actual boundary conditions.

Figure 3.16 shows load-strain curves corresponding to Concept 4. Figure 3.16(a), which is the glass fiber top skin, shows that experiment results differ little from the simply-supported FEM simulation. This confirms that the experiment was predominantly simply-supported, as intended. Figure 3.16 (b), CFRP bottom skin, is not conclusive, because experimental results are nonlinear. Figure 3.17 corresponds to Concept 3. The simulation curves between fully CC and SS-SS BCs are almost the same, because the structures are symmetric about top and bottom skins, but failure firstly starts at SS-SS BC because it is rotation-free. The simulation results overlay the experiment results except one, demonstrating the accuracy of results. Boundary condition of the experiment was suspected as the cause of the nonlinearity.

Table 3.3. SWASS compression test panel

ID	Bottom Skin (SG1)	Top Skin (SG2)	Tube wrap	Length (in (mm))	Width (in mm))	Total Height (in (mm))
6	5 Ply(*) 660 CFRP	5 Ply E-Glass	2 Ply Biaxial Fiberglass	2.12 (53.8)	3.129 (79.5)	0.435 (11.0)
7	5 Ply 660 CFRP	5 Ply E-Glass	2 Ply Biaxial Fiberglass	2.15 (54.6)	3.134 (79.6)	0.435 (11.0)
9	5 Ply 660 CFRP	5 Ply E-Glass	2 Ply Biaxial Fiberglass	2.13 (54.1)	3.088 (78.4)	0.435 (11.0)
8	5 Ply E-Glass	5 Ply E-Glass	2 Ply Biaxial Fiberglass	2.088 (53.0)	3.160 (80.2)	0.428 (10.9)
10	5 Ply E-Glass	5 Ply E-Glass	2 Ply Biaxial Fiberglass	2.1 (53.3)	3.137 (79.7)	0.424 (10.8)

(*): All 5 ply laminates are 0/90, ±45, 90/0, ±45, 0/90

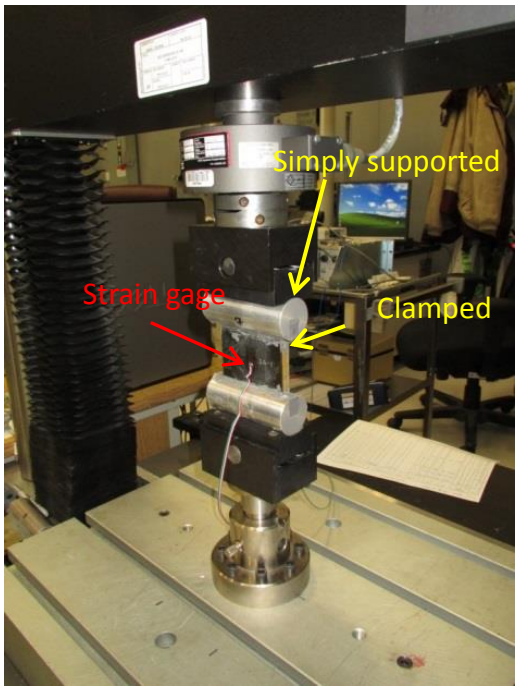

Figure 3.15. MTS compressive load test (ASTM C364)

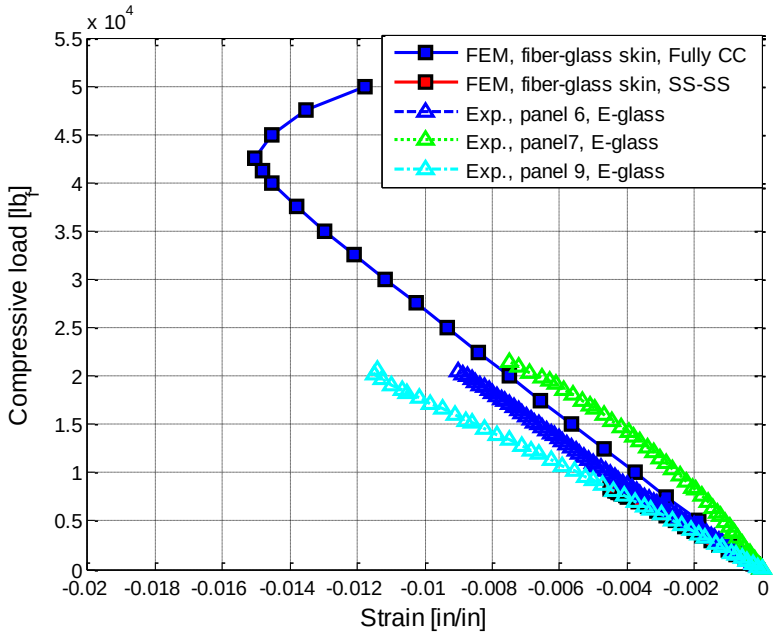

(a) E-glass top skin

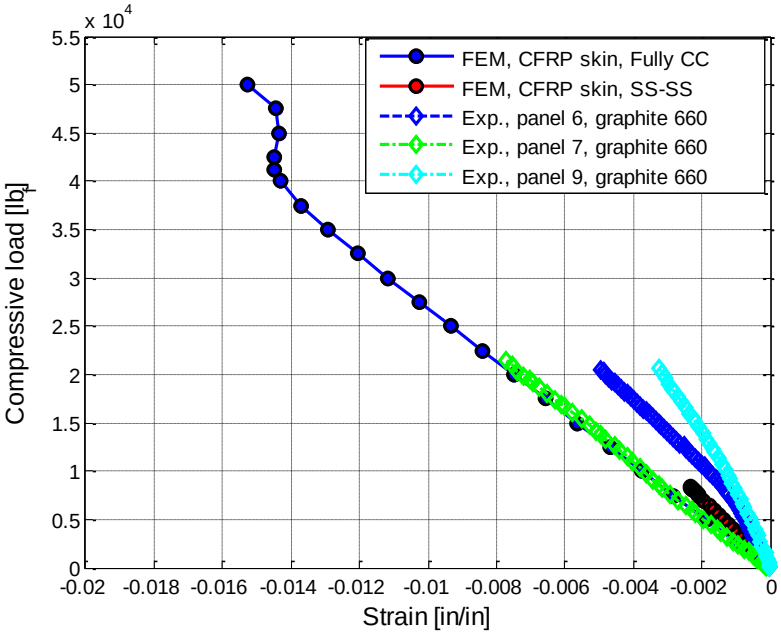

(b) CFRP bottom skin

Figure 3.16. Comparison of fiber direction strains: 5ply E-glass on both sides (1000 lb_f = 4.45kN)

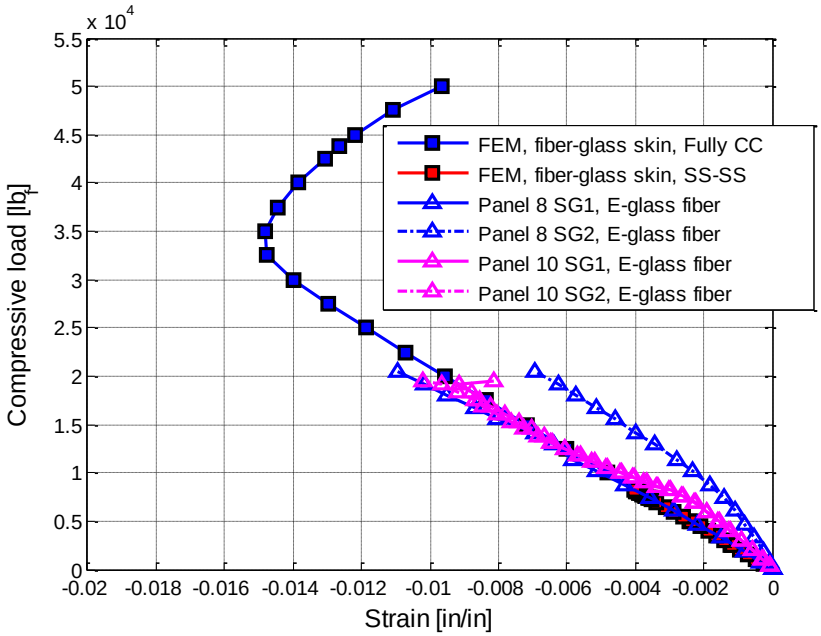

Figure 3.17. Comparison of fiber direction strains: 5ply E-glass on both sides (1000 lb_f = 4.45kN)

3.6 Conclusions and Future Work

AFRL and Virginia Tech research team has proposed and developed the SWASS configured as composite waveguide tubes covered by electromagnetically transparent or non-electro-magnetically transparent laminate skins. The tubes can be replaced with metallic foil for the alternative design to improve EM radiation performance. These composite structures are critical not only for structural weight to be reduced but also for structural strength to be reinforced. This research presents structural design and optimization of the four novel SWASS design concepts. The equivalent model was proposed and compared to an analytical approach. This method is important in that it is cost-effective by simplifying 3D structure into 2D plate model to indicate rough trends, but also leads to substantial approximation error when smearing the effect of slots. For higher fidelity, 3D plate FEM models for these structures are proposed to save computational cost, while maintaining accuracy. Nonlinear strain test evaluated the mechanical failure and lightweight design criteria and provided optimal design solutions. It was shown that concept 1 (CFRP WG) and concept 4 (CFRP + Copper WG) are good; Concept 4 may be best in both structural and EM efficiencies. The 3D modeling was validated against experiments. They were in good agreement in some cases, but there are still a few uncertainties such as BCs, bonding strength of layers, etc. For future work, we propose research that will continue to optimize simultaneously the structural and electromagnetic performance.

Chapter 4 Distributed Computation for Design Optimization of Aircraft

Garrett Hehn, Robert A. Canfield, and Woon Kim
Dept. of Aerospace and Ocean Engineering, Virginia Tech, Blacksburg, VA

4.1 Introduction

The objective of this study is to utilize the Service Oriented Computing Environment (SORCER) program provided by the U.S. Air Force Multidisciplinary Sciences and Technology Center for the creation of an optimum aircraft design [23, 24]. The SORCER program allows for the distribution of tasks across its network; critical analysis can be requested by a user and performed on any capable machine on the network. Services on the network accept variables that describe a physical model, called design variables, implement the analysis, and return the analysis results. Most methods of design optimization require that the change in the results of the analysis due to the change of each design variable, or gradient, be calculated. With distributed computing, complex models with any number of design variables, thus requiring countless iterations for optimization, can be performed quickly and efficiently; SORCER makes the optimization of large scale design problems possible. Additionally, the network allows for collaboration on a large scale; the expertise of one party can be used to benefit the entire network. To demonstrate these capabilities and advantages, Ricciardi's Nonlinear Aeroelastic Scaling [43, 44] procedure was created in the SORCER environment. An additional benefit to this project was achieved due to the relative programming inexperience of the author; included in this report is my preparation for creating in the SORCER environment as well as recommendations for beginning users and SORCER administrators alike.

4.2 Project Description

The procedure implemented in the SORCER environment was created by Anthony Ricciardi of Virginia Tech. This procedure was motivated by the need for a scaled model that exhibited the predicted nonlinear response phenomena. This model would provide verification of several design features at a significantly lower cost than larger scale or full scale model. Due to manufacturer and material constraints, as is often the case, a simple geometric scaling could not be performed; instead a new internal structure would be designed. Optimization of this new internal structure was performed to generate the best design that also ensured strict adherence to the desired nonlinear response phenomena. This was achieved using the method of Equivalent Static Loads (ESL) as detailed by Park *et al* [45]. A visualization of this method is shown in Figure 4.1, given an initial design and load case, first nonlinear static analysis is performed to determine the nonlinear response. Given the nonlinear response, equivalent static forces are calculated to achieve such a response. Then, linear optimization of the design is performed using the equivalent static forces. The new linearly optimized design is then used to repeat the process until the optimum design is reached. ESL optimization is available within MacNeal-Schwendler Corporation (MSC) Nastran; however, with significant drawbacks. For example, Nastran cannot impose the simultaneous constrain on modal frequencies. These difficulties motivated Ricciardi to develop a process to be implemented through Matlab. This "wrapper" of several of Nastran's abilities was the basis of the SORCER implementation detailed in this report.

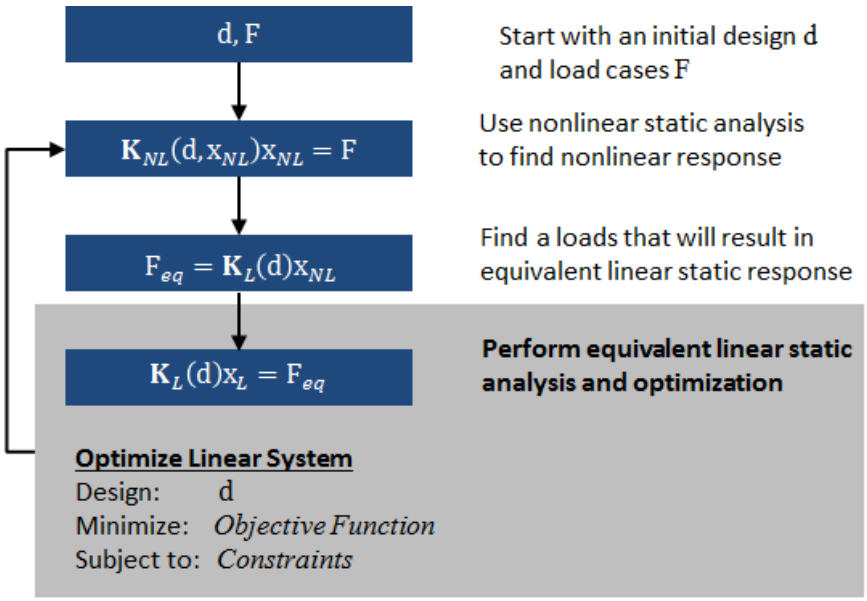

Figure 4.1. Flowchart of Equivalent Static Loads optimization [45] provided by Anthony Ricciardi.

4.3 Background Work

Before describing the implementation of this project in SORCER, it is of value to describe the preparation beneficial to one lacking extensive programming experience beyond an introductory course for C++ and regular use of Matlab for most of computations. Most notably, this section benefits an engineer with no experience in Java. The lectures provided for the course *Introduction to Computer Science: Programming Methodology* taught by Dr. Mehran Sahami of Stanford were the most valuable. All the course materials, lectures included, are provided freely at the link provided at the end of this report in Section 4.7. This course offers a very accessible introduction to basic programming methods: an excellent resource for complete beginners to programming as well as novices. The largest benefit of the course was the introduction to object oriented programming. After the Stanford course, another tutorial was completed concerning the software Eclipse, the software used for Java source code development in the SORCER environment. The link to this tutorial is provided as well. The main benefit of this tutorial was the insight gained into the built in tools of Eclipse. For example, when Eclipse flags an error several "Quick Fix" options are suggested. For a programming novice inexperienced with Java, the listed "Quick Fix" options are helpful in first understanding the error and sometimes providing a solution. The "Quick Fix" option is not to be relied upon exclusively, but with understanding of its abilities it is a very helpful debugging tool.

Inside the SORCER registry, there are several helpful examples of note. First, the *Hello World* example is an excellent starting point. Most simply, it provides verification that SORCER has been properly configured to the present machine; the necessary changes to the sorcer.env file and that the correct boot process has been performed. Additionally, it familiarizes the user with the somewhat foreign idea of "publishing" services or providers to the SORCER browser. Second, example 6, an arithmetic example, is a worthwhile exercise. It introduces the ANT files well and an important lesson can be learned from spending time in the example; it is often not necessary to change the source code, but to understand the requester or provider it is often

necessary to examine the source code. This example also highlights the information that can be gained from the console window. The arithmetic output is displayed in this window. Creating additional run files to explore all the abilities available via the common requester source code, starting with this example, is recommended. Lastly, the *XYZprovider* under the "scott" folder in the "examples" folder is useful to introduce the user to the Context class, most often used to pass data. The user also learns how data can be passed by URL from provider to requester or task to task.

4.4 Implementation in SORCER Environment

4.4.1 Example of nonlinear aeroelastic scaling model

Ricciardi's Nonlinear Aeroelastic Scaling procedure connects well to the idea and syntax of the SORCER environment. The multiple calls to Nastran, each time with a different executive control, can be accomplished by assembling a Nastran job with multiple tasks. Equivalent static loads output is easily passed back into the requester directory by URL. The parsing of output files for the new design or for calculation of the objective function makes use of the extensive filters already in place in SORCER.

The specific flow of how Ricciardi's Nonlinear Aeroelastic Scaling procedure is formatted in the SORCER environment can be seen in Figure 4.2. It should be noted that this particular model and load case had been previously tested and shown to converge within four iterations. Therefore, a for loop structure is used instead of a while loop with an optimality test. The analysis requires the following input files in directory indicated in the properties file: NL_Static_ESL.dat, L_Static_opt.dat, Analysis_Lin.dat, Analysis_NL.dat, model_N.bdf, target_airloads.bdf, target_gravityloads.bdf, Obj_statics.bdf, nl_static_esl_esl.blk. All of the files with the extension ".dat" contain executive control commands defining the specific solution to be acquired in Nastran. The files with the extension ".bdf" are bulk data files containing the model structure and loads subjected to the model and are used for every Nastran task with the exception of Obj_statics which is only used in the first and second Nastran tasks. The final file, nl_static_esl_esl.blk, doesn't need to be in the requester directory; it is generated after the first Nastran task.

This first task, the first block within the loop on Figure 4.2 labeled Nastran, calculates the nonlinear response and calculates the equivalent static loads to match such a response. These equivalent static loads are output into a file with the same name as the main input file, in this case NL_Static_ESL.dat, except with the extension "_esl.blk" and all lower case letters, hence the name nl_static_esl_esl.blk. The correct file name of this output file must be given in the properties file for the output file to be correctly identified and moved into the requester directory to be used in subsequent Nastran runs.

The second Nastran task, the second block within the loop on Figure 4.2 labeled Nastran, uses the newly calculated equivalent static loads to linearly optimize the design. The main input file for this task is L_Static_opt.dat. The resulting punch file of the same name, again all lower case letters, is parsed and the new design is located. Once the new design is located, it is stored and placed into the file model_N.bdf, after the previous design had been wiped from the file.

The last two Nastran tasks calculate the linear response, using the main input file Analysis_Lin.dat, and nonlinear response, using the main input file Analysis_NL.dat, of the new design. When parsed, the response data provided by these final two runs is used to calculate the difference between the new design response and the target predicted response. This difference defines the objective function for the design.

In order to allow several Nastran tasks, each with different main input files, the source code of the nastranRMK requester was modified. A new main method was added to include the previously described loop structure containing the four Nastran tasks. Additionally, the method to create the Context and call Nastran was modified to include a decision structure that chose the correct main input files and bdf files based on a string passed to the method. Within the Java source code, several methods were also added to help parse the output, search for the new design, and store the new design. Outside of the Java source code, the only changes required were the addition of several new fields in the properties file so that all the necessary files could be identified for the requester.

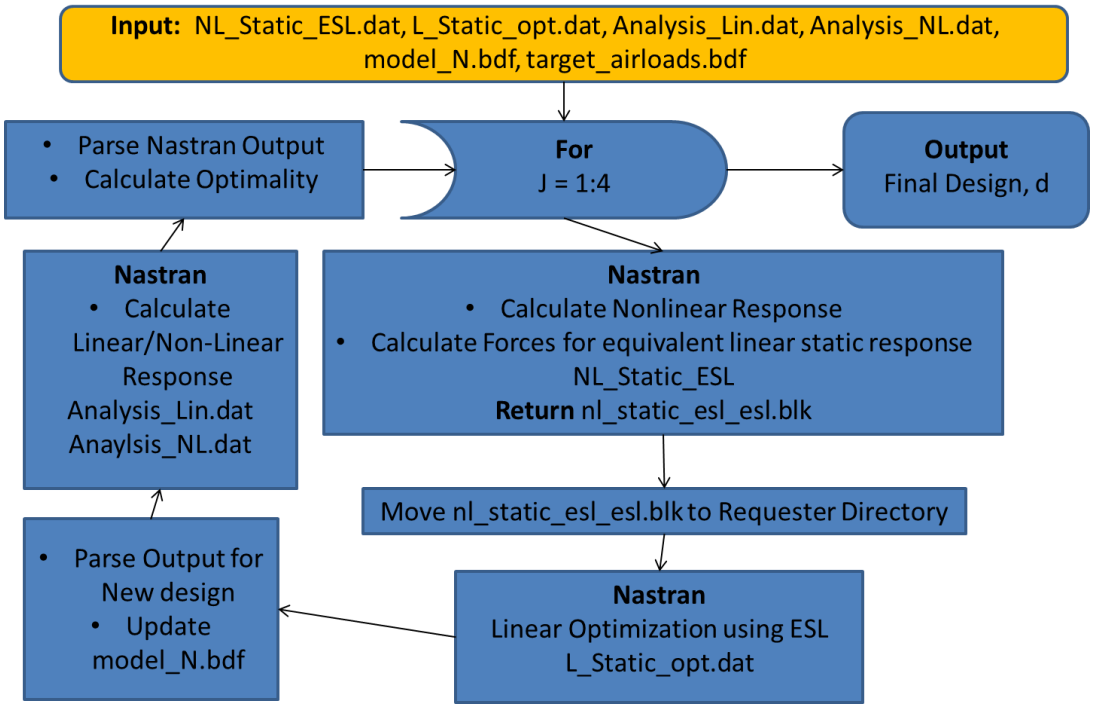

Figure 4.2. Flowchart of Ricciardi's Nonlinear Aeroelastic Scaling procedure within the SORCER environment

4.4.2 Example of SWASS structural model

The MDO of SWASS will be enhanced with an online computational framework based on global network system which integrates multiple computational tools. This task will be computationally intensive, but the Service Oriented Computing Environment (SORCER) provided by the U.S. Air Force's Multidisciplinary Sciences and Technology Center (MDTC) shows a great promise for this purpose. We propose to continue the use of SORCER initially explored for SWASS MDO in our recent preliminary effort as illustrated in Figure 4.3.

 # nastran files
requestor.nastran.inputfile=3
DC1 BUCK fullvCC.dat

provider.nastran.execommand=C:/MSC.Software/MSC_Nastran/20122/bin/nastran batch=no

1 LINEAR BUCKLING
R E A L E I G E N V A L U E S

MODE NO.	EXTRACTION ORDER	EIGENVALUE
1	**1**	**2.394260E+04**
2	2	2.425010E+04
3	3	2.488814E+04

(a) Requestor and executable provider command scripts in order to get buckling output

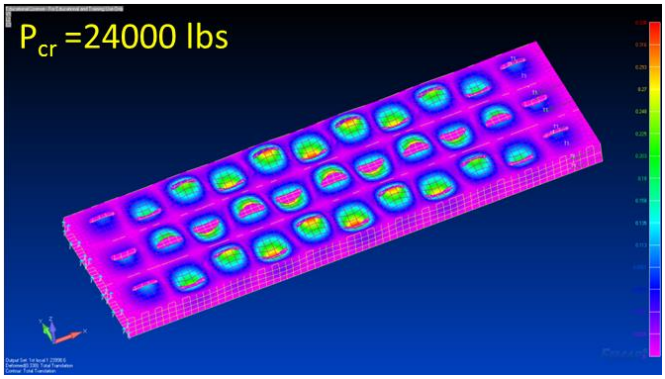

(b) 1st buckling mode output from FEMAP (NX NASTRAN solver) [41]

Figure 4.3. Example of SWASS structural response using the SORCER, demonstrating the buckling of Concept 1

4.5 Current Issues and Future Work

The procedure described was originally implemented as a separate module that utilized the *nastranRMK* provider. However, difficulties with the ANT build file led to the direct modification of the *NastranRequester.java* file within the *nastranRMK* requester package. Currently, the first Nastran task is being completed, but no "_esl.blk" file is output. This problem is likely a result of an error within the NL_Static_esl.dat file. Additionally, after this first task, no more tasks are attempted or completed. The console window indicates an "Exception in thread "main" java.lang.NoClassDefFoundError: org/jfree/chart/axis/ValueAxis." There is no console activity that indicates the second Nastran task is initiated; there is no output detailing the creation of the Context that is usually present. Due to this error, the parsing, searching and storing for the new design have yet to be verified. In addition, parsing for the purpose of the calculation of the objective function for the design has not been implemented.

This last piece of parsing to be implemented should take into consideration the following information about filters within SORCER. There are several valuable methods, *String.split* and

regx, within *NastranOutput.java* a class within the *nastranRMK* provider package. Currently, this class is configured to parse static and dynamic aeroelastic results and place them into a *NastranObject* object. This method is the best candidate to be extended for the purposes of this project. Additionally, in the *BasicFileFilter* class is the *.getFields* method which allows parsing of bulk data with a comma or fixed field length. Modification to allow the input of the proper delimiter could make this method viable as well. For further reference, the package containing all basic filters is located in the directory "iGrid/modules/sorcer/src/sorcer/vfe/filter/." With this information concerning filters and resolution of the previously stated error, this module can likely be completed, tested and committed to the registry in the near future.

4.6 Conclusion

This project sought to highlight the advantages of the SORCER environment by implementing Ricciardi's Nonlinear Aeroelastic Scaling procedure within the SORCER environment. Though the module to perform this analysis is not completely finished, the advantages of SORCER are still apparent. A large library of modules for most aerospace applications already exists. Built in filters and similar methods provide reading and writing assistance for a variety of file types and formats. Making full use of the already established and functioning modules and examples is recommended for a beginning user; most only require a few changes in the property files to allow provider and requester to be run from one's machine. If there is existing source code that can be modified to fit user needs, always modify before attempting to create a module from scratch. At the very least, one can fall back upon the *serviceProvider_Requester_Template* package located in the directory "iGrid/modules/engineering/apps/." With these resources and the necessary background knowledge, most should be able to create and utilize the SORCER environment.

The most difficult part of implementing or simply using existing modules within SORCER was locating them. Neither the package explorer nor navigator tabs within Eclipse allowed for easy navigation or search. This problem was only compounded by the manual which often had blank sections (Java Native Access sections) and was far too technical for a typical engineer's entry level of knowledge. Additionally, the wealth of presentations in the notes section were helpful, but often had large amounts of crossover material and required significant time to comb through to find useful information. The SORCER environment would benefit greatly from a centralized index. At the least, the index could include all modules currently available and functioning along with a short description of its purpose or abilities. A longer description which described methods or filters developed within the module would also be appreciated. The most helpful would be instructions of what the user needs to provide or alter. For example, the *readME.txt* document included in the module titled "nastran" under "requester/docs" was very helpful. It is a short paragraph that informs the user of what must be supplied. Ideally, both the index and every module in the "docs" folder would have a similar paragraph. If such an index were to be appended to a complete manual which can provide more in depth information for more experienced user, the SORCER environment would become more accessible to all users.

4.7 Tutorial Links

Stanford's Introduction to Computer Science: Programming Methodology:
<http://see.stanford.edu/see/courseinfo.aspx?coll=824a47e1-135f-4508-a5aa-866adcae1111>
Eclipse Online Tutorial:
<http://eclipsetutorial.sourceforge.net/totalbeginnerlessons.html>

Chapter 5 Conclusions and Recommendations

Conclusions

The SWASS was configured by multiphysics modeling to quantify the variation in structural and electromagnetic performance. This study was accompanied with trade studies involving structural parameters such as panel thickness, composite laminate layup, stiffener size, shape and spacing, as well as waveguide parameters such as slot size, and spacing. The achievements are summarized as follows.

- Formulated an integrated multidisciplinary design optimization (MDO) problem statement that incorporates the multiple objectives of minimizing structural mass and maximizing EM beam intensity, while satisfying structural constraints on strength and stiffness and EM constraints on EM beam width, direction and actuating power. Solved the EM sub-problem initially using RSM.

- Finite difference sensitivity calculations were implemented for the aforementioned SWASS configurations to confirm the extent to which optimality conditions were satisfied by the approximate optimal designs found using RSM. The computed sensitivities in gradient-based optimization methods were used to hone in on locally optimal solutions.

- Structural design and optimization of the four novel SWASS design concepts were performed. Classical composite plate theory was employed to construct the equivalent plate model accompanying smeared effect of slots. For higher fidelity, 3D plate FEM models were developed for computational cost savings, while maintaining accuracy. The 3D models were validated against experiments. Computational models and source for SWASS design optimization were delivered that are compatible and functions with Service ORiented Computing EnviRonment (SORCER).

Recommendations

In order to advance the multiple structural and EM performances, we propose an integrated approach to a technology solution for SWASS:

(1) Formulate the parameterization scheme for SWASS design that enhances the combined electromagnetic and structural performance. This will lead designers to direct the development by requests of AFRL.

(2) Develop an analytical/numerical methodology that will enable predictions of the complex radiation patterns. The new methodology, based on a mathematical framework for establishing and unifying the existing solutions, will compute numerically the multiobjective optimal problems.

(3) Develop software that integrates low and high complexity design and optimization. The software shall be appropriate for use by SWASS developers and accommodate progressive design by use of the SORCER consistent with the system-level design requests.

Acknowledgement

This material is based on research sponsored by the Air Force Research Laboratory under the agreement number FA8650-09-2-3938. The U.S. Government is authorized to reproduce and distribute reprints for governmental purposes notwithstanding any copyright notation thereon.

Regarding the SORCER, the authors would like to thank all those who offered assistance to this project both at Virginia Tech and at AFRL. Special thanks are due to the following: Scott Burton of AFRL for all the help debugging, Dr. Raymond Kolonay of AFRL for the valuable insight on filters, Anthony Ricciardi for providing background on ESL and his process and Nathan Love who provided the Stanford tutorial.

List of References

1. Paul, D., Kelly, L., Venkayya, V., and Hess, T., *Evolution of U.S. military aircraft structures technology.* Journal of Aircraft, 2002. **39**(1): p. 18-29.
2. Callus, P.J., *Conformal Load-Bearing Antenna Structure for Australian Defence Force Aircraft*. 2007: Australia. p. 50p.
3. Lockyer, A.J., Alt, K.H., Coughlin, D.P., Durham, M.D., Kudva, J.N., Goetz, A.C., and Tuss, J. *Design and development of a conformal load-bearing smart-skin antenna: overview of the AFRL Smart Skin Structures Technology Demonstration (S3TD)*. in *Smart Structures and Materials 1999: Industrial and Commercial Applications of Smart Structures Technologies, 2-4 March 1999*. 1999. USA: SPIE-Int. Soc. Opt. Eng.
4. Alt, K.H., Lockyer, A.J., Coughlin, D.P., Kudva, J.N., and Tuss, J. *Overview of the DoD's RF Multifunction Structural Aperture (MUSTRAP) Program*. in *Smart Structures and Materials 2001: Smart Electronics and MEMS, 5-7 March 2001*. 2001. USA: SPIE-Int. Soc. Opt. Eng.
5. Smallwood, B.P., Canfield, R.A., and Terzuoli Jr, A.J. *Structurally integrated antennas on a joined-wing aircraft*. in *44th Structural Dynamics, and Materials Conference*. 2003. Norfolk, VA, United states: American Inst. Aeronautics and Astronautics Inc.
6. Seong Ho, S., Soon Young, E., and Woonbong, H., *Development of a smart-skin phased array system with a honeycomb sandwich microstrip antenna.* Smart Materials and Structures, 2008. **17**(Copyright 2008, The Institution of Engineering and Technology): p. 035012 (9 pp.).
7. Skolnik, M.I., *Radar handbook*. 1990, New York: McGraw-Hill.
8. Stimson, G.W., *Introduction to Airborne Radar (2nd Edition)*. SciTech Publishing.
9. *List of Radars*. cited 04-19-2010; Available from: http://en.wikipedia.org/wiki/List_of_radars.
10. Collin, R.E., *Foundations for Microwave Engineering (2nd Edition)*. Wiley-IEEE Press.
11. Balanis, C.A., *Antenna Theory - Analysis and Design (3rd Edition)*. 2005: John Wiley & Sons.
12. Callus, P.J., *Novel Concepts for Conformal Load-Bearing Antenna Structure*. 2008: Australia. p. 111p.
13. Johnson, R.C., *Antenna Engineering Handbook (3rd Edition)*. 1993: McGraw-Hill.
14. Bushnell, D., *Theoretical basis of the PANDA computer program for preliminary design of stiffened panels under combined in-plane loads.* Computers and Structures, 1987. **27**(Copyright 1988, IEE): p. 541-63.
15. Changyi Su, H.K., Todd Hubing, *Overview of Electromagnetic Modeling Software*, in *25th Annual Review of Progress in Applied Computational Electromagnetics* 2009: Monterey, California.
16. *RF Module User's Guide*. 2010, COMSOL Multiphysics.
17. EMSS, *FEKO User's Manual*. 2013, EM Software & Systems-S.A. (Pty) Ltd.
18. *CST MICROWAVE STUDIO* cited 04-05-2010; Available from: https://www.cst.com/.
19. *ANSYS HFSS*. cited 04-05-2010; Available from: http://www.ansys.com/.
20. *edaboard*. cited 04-05-2010; Available from: http://www.edaboard.com/.
21. E. Johansson, N.K.-W., C. Wikstrom, and S. Wold L. Ericksson, *Design of experiments: principles and applications*. 2000: Umetrics Academy.

22. Canfield, R.A., *Multipoint cubic surrogate function for sequential approximate optimization.* Structural and Multidisciplinary Optimization, 2004. **27**(5): p. 326-336.
23. Kolonay, R.M. and Sobolewski, M., *Grid Interactive Service-Oriented Programming Environment*, in *11th ISPE International Conference on Concurrent Engineering: Research and Applications (CE2004)*. 2004: Beijing, China. p. 90-102.
24. Soblewski, M. *SORCER: Computing and metacomputing intergrid*. in *ICEIS 2008. Tenth International Conference on Enterprise Information Systems, 12-16 June 2008*. 2008. Madeira, Portugal: Institute for Systems and Technologies of Information, Control and Communication.
25. Ha, T. and Canfield, R.A. *Design Optimization of a WR-90 Slotted Waveguide Antenna Stiffened Structures* in *52nd AIAA/ASME/ASCE/AHS/ASC Structures, Structural Dynamics and Materials Conference, April 4, 2011 - April 7, 2010*. 2011. Denver, CO, United states: American Institute of Aeronautics and Astronautics Inc.
26. Callus, P.J., *Novel Concepts for Conformal Load-Bearing Antenna Structure*. 2008, Defense Science and Technology Organization, Aeronautical and Maritime Research Laboratory, P.O. Box 4331, Melbourne, Victoria, 3001, Australia. p. 94.
27. Sabat, J.W. and Palazotto, A.N., *Structural performance of composite material for a slotted waveguide antenna stiffened structure under compression.* Composite Structures, 2013. **97**( ): p. 202-210.
28. Kim, W., Canfield, R.A., Baron, W., Tuss, J., and Miller, J. *Modeling and Simulation of Slotted Waveguide Antenna Stiffened Structures*. in *19TH INTERNATIONAL CONFERENCE ON COMPOSITE MATERIALS*. 2013. Montreal, Canada: .
29. Volakis, J.L., *Antenna engineering handbook*. 2007, New York: McGraw-Hill.
30. Balanis, C.A., *Advanced engineering electromagnetics*. 1989, New York: Wiley.
31. Elliott, R.S., *Antenna theory and design*. 2003, Hoboken, N.J.: John Wiley & Sons.
32. MATLAB, *Optimization ToolboxTM User's Guide*. 2012.
33. ModelCenter, *ModelCenter 8.0 Help*. 2008, Phoenic Integration, Inc.
34. Eriksson, L., Johansson, E., Kettaneh-Wold, N., Wikström, C., and Wold, S., *Design of Experiments: Principles and Applications*. 2000: Umetrics Academy.
35. Myers, R.H.M., Douglas C.; Anderson-Cook, Christine M., *Response surface methodology : process and product optimization using designed experiments*. 2009, Hoboken, N.J.: Wiley.
36. Kim, W., Ha, T., Canfield, R.A., Baron, W., and Tuss, J., *Radio Frequency Optimization of Slotted Waveguide Antenna Stiffened Structure* In preparation.
37. Knutsson, L., Brunzell, S., and Magnusson, H. *Mechanical design and evaluation of a slotted CFRP waveguide antenna*. in *Fifth International Conference on Composite Materials, ICCM-V*. 1985. San Diego, CA, USA: Metallurgical Soc Inc.
38. Timoshenko, S. and Woinowsky-Krieger, S., *Theory of plates and shells*. 1959, New York: McGraw-Hill.
39. Gürdal, Z., Haftka, R.T., and Hajela, P., *Design and optimization of laminated composite materials*. 1999, New York: Wiley.
40. Reddy, J.N., *Mechanics of laminated composite plates and shells : theory and analysis*. 2nd ed. 2004, Boca Raton: CRC Press.
41. *FEMAP 10.3*. 2011, Siemens Inc.
42. *MSC Nastran Quick Reference Guide 2012*, in 2012, MSC Software.

43. Ricciardi, A.P., Canfield, R.A., Patil, M.J., and Lindsley, N. *Nonlinear aeroelastic scaling of a joined-wing aircraft*. in *53rd AIAA/ASME/ASCE/AHS/ASC Structures, Structural Dynamics and Materials Conference, April 23, 2012 - April 26, 2012*. 2012. Honolulu, HI, United states: American Institute of Aeronautics and Astronautics Inc.
44. Ricciardi, A.P., Eger, C.A.G., Canfield, R.A., and Patil, M.J. *Nonlinear aeroelastic scaled model optimization using equivalent static loads*. in *54th AIAA/ASME/ASCE/AHS/ASC Structures, Structural Dynamics and Materials Conference, April 8, 2013 - April 11, 2013*. 2013. Boston, MA, United states: American Institute of Aeronautics and Astronautics Inc.
45. Park, G.-J., Shin, M.-K., and Park, K.-J., *Optimization of structures with nonlinear behavior using equivalent loads.* Computer Methods in Applied Mechanics and Engineering, 2007. **196**(4-6): p. 1154-67.

Appendix A. Electromagnetic Part

A.1 Electromagnetic Convergence Study

Higher electromagnetic frequencies require finer finite element meshes for analysis. According to the Nyquist criterion, the maximum mesh size should be no more than a fraction of a wavelength. For 10GHz this criterion conservatively dictates the largest element dimension be no more than 0.003m to analyze the antenna. However, a convergence study revealed that a mesh with a maximum element dimension of 0.014m was sufficient to accurately simulate far field strength of the WR-90 slotted waveguide antenna. For the design optimization the objective will be to maximize the peak magnitude in the electric field. Therefore, it is the primary criterion for assessing convergence. As shown in Table A. 1, there are significant differences on the peak magnitude in going from the coarsest mesh to the nominal mesh, whereas there is no noticeable difference in peak magnitude between the nominal and finer meshes. Effect of mesh resolution on convergence of finite difference derivatives is a subject of future research. Pending that study, the minimal mesh is considered adequate for the preliminary optimization studies.

Table A. 1 Convergence of meshes

Resolution	Model	Radiation Pattern	Mesh size	Elements
Coarser	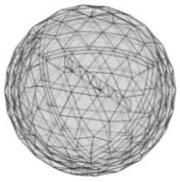	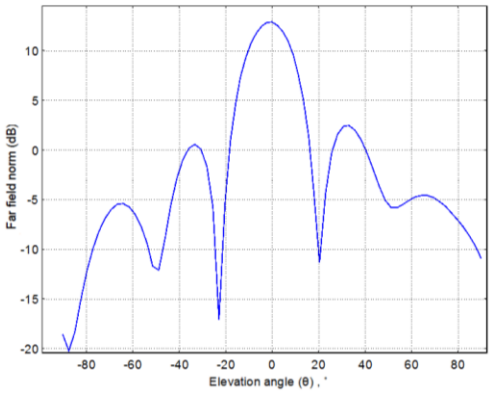	0.0266m	4,288
Coarse	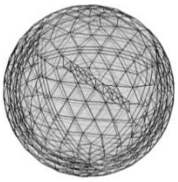	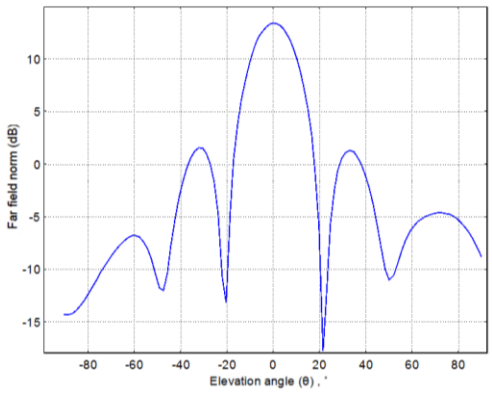	0.021m	6,879

Nominal	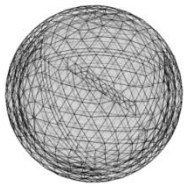	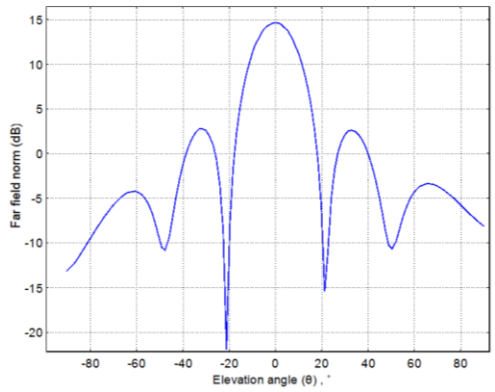	0.014m	12,807
Fine	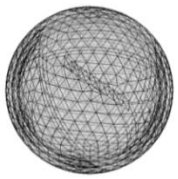	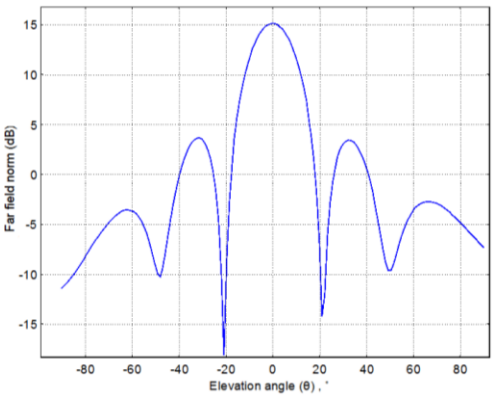	0.0112m	21,205
Finer	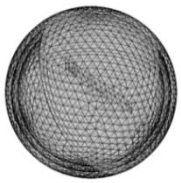	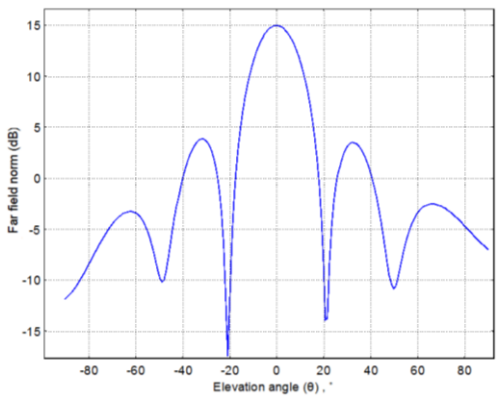	0.0077m	51,642
Extra fine	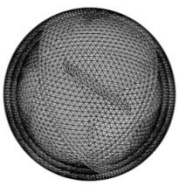	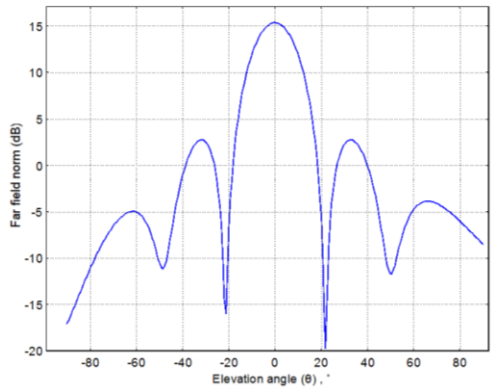	0.0049m	201,412

A.2 Types of Rectangular Waveguide Standards

Table A. 2. Rectangular waveguide standards

Frequency band	Waveguide standard	Frequency limit (GHz)	Dimensions Width × Height (inches)	Dimensions Width × Height (m)
F	WR-159	4.90–7.05	1.590 × 0.795	0.04039 × 0.02019
C	WR-137	5.85–8.20	1.372 × 0.622	0.03485 × 0.01580
H	WR-112	7.05–10.0	1.122 × 0.497	0.02850 × 0.01262
X	WR-90	8.20–12.4	0.900 × 0.400	0.02286 × 0.01016
Ku	WR-62	12.4–18.0	0.622 × 0.311	0.01580 × 0.07900
K	WR-51	15.0–22.0	0.510 × 0.255	0.01295 × 0.00648
K	WR-42	18.0–26.5	0.420 × 0.170	0.01067 × 0.00432
Ka	WR-28	26.5–40.0	0.280 × 0.140	0.00711 × 0.003556

Appendix B. Structural Part

B.1 Buckling Analysis of Non-slotted and Slotted Waveguide Tubes

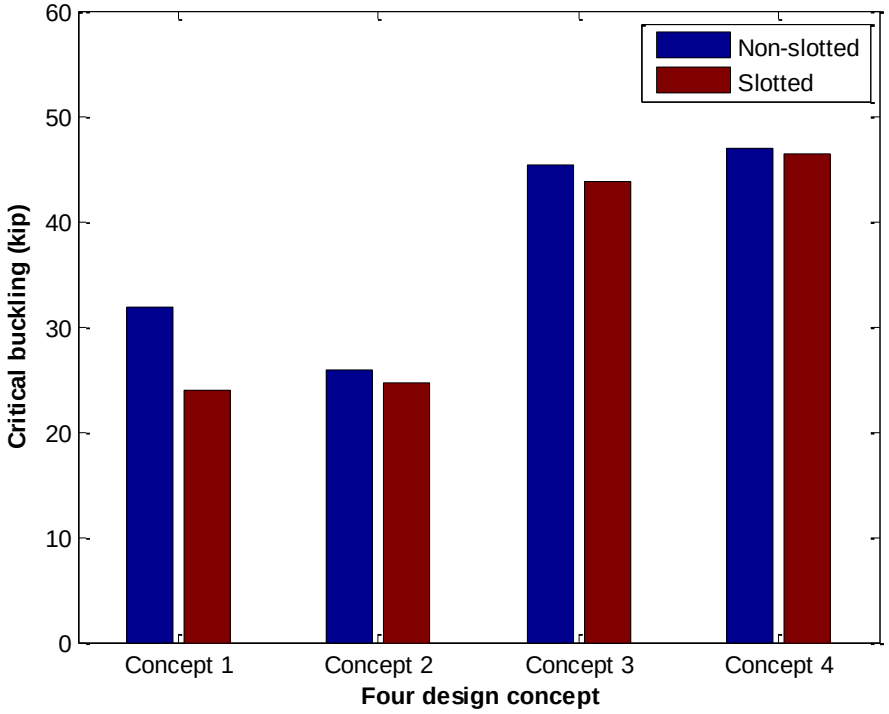

Figure B. 1. Comparison of non-slotted and slotted waveguide tubes.

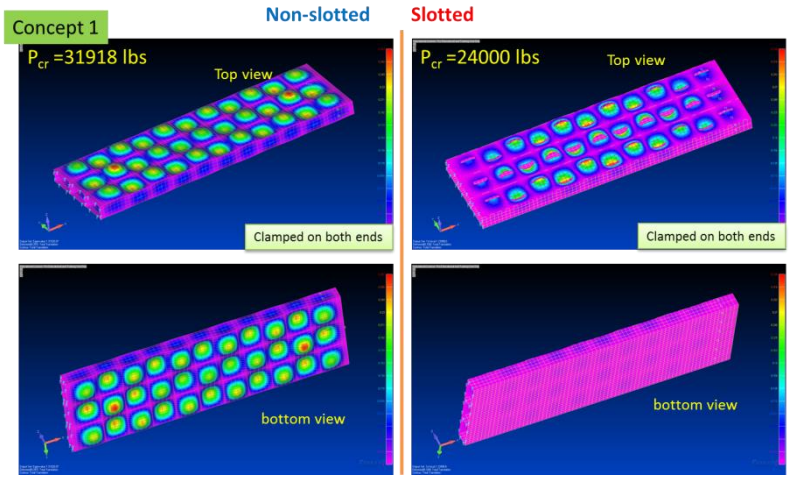

(a) Concept 1

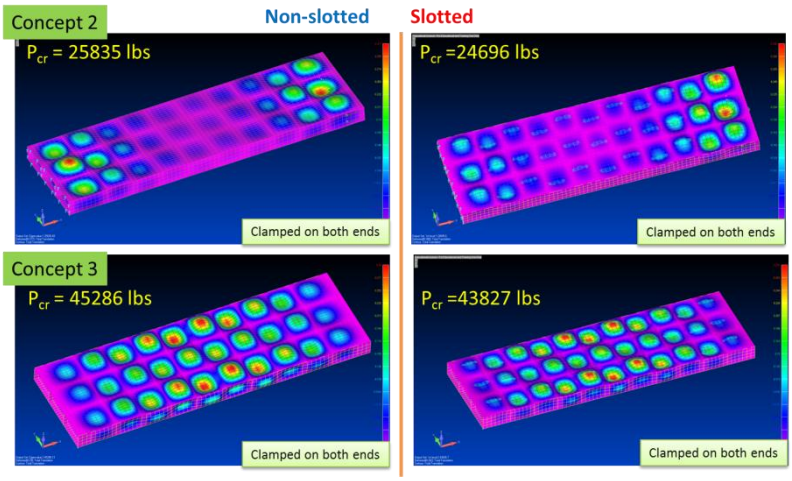

(b) Concepts 2 & 3

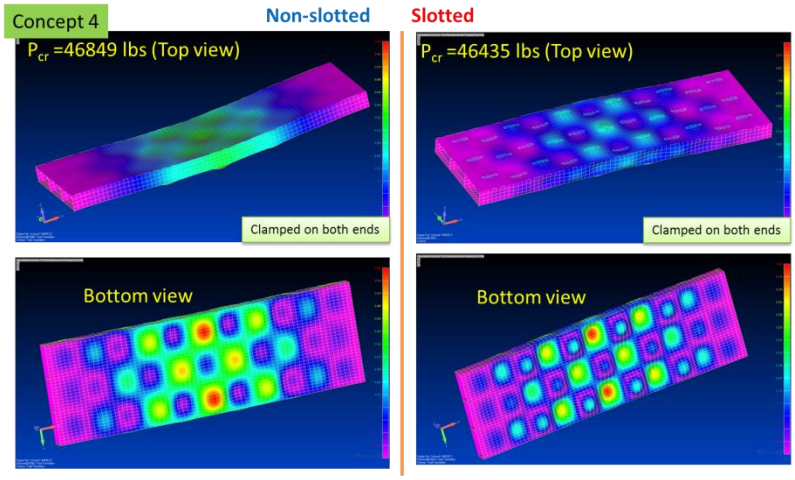

(c) Concept 4

Figure B. 2. Buckling modes of non-slotted and slotted waveguide tubes.

B.2 Interlaminar Shear Stresses

(a) Concept 1

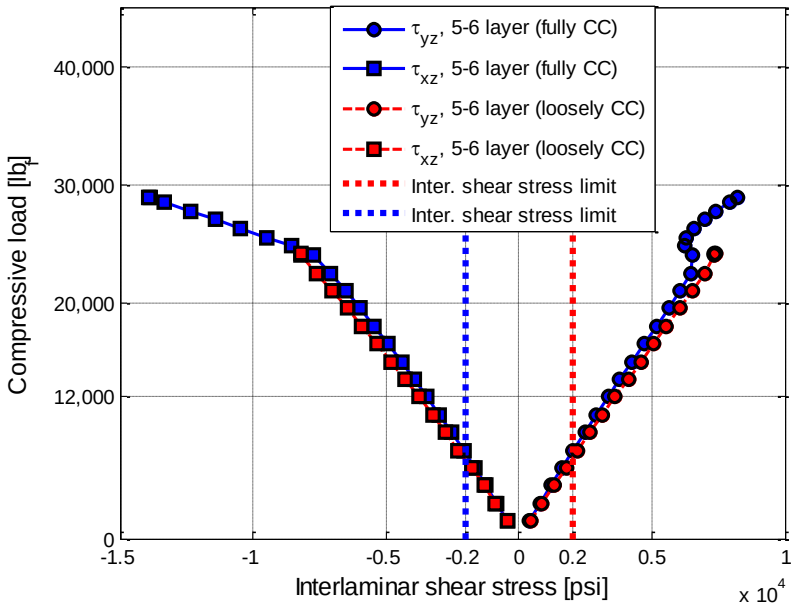

(a) Initial design

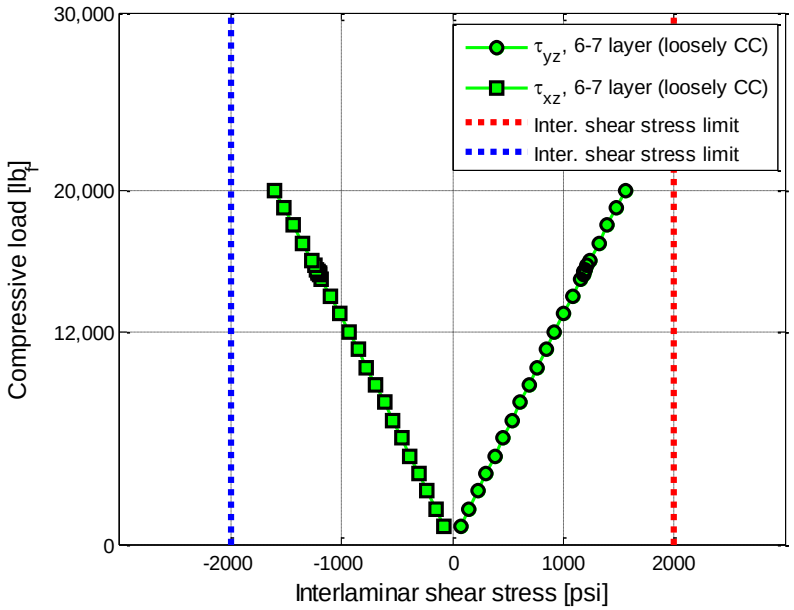

(b) Post-optimization

Figure B. 3. Concept 1: Interlaminar shear stress curves. The post-optimization curves satisfy the interlaminar shear stress requirements at the design load of 12,000 lb_f (see Chapter 3).

(b) Concept 2

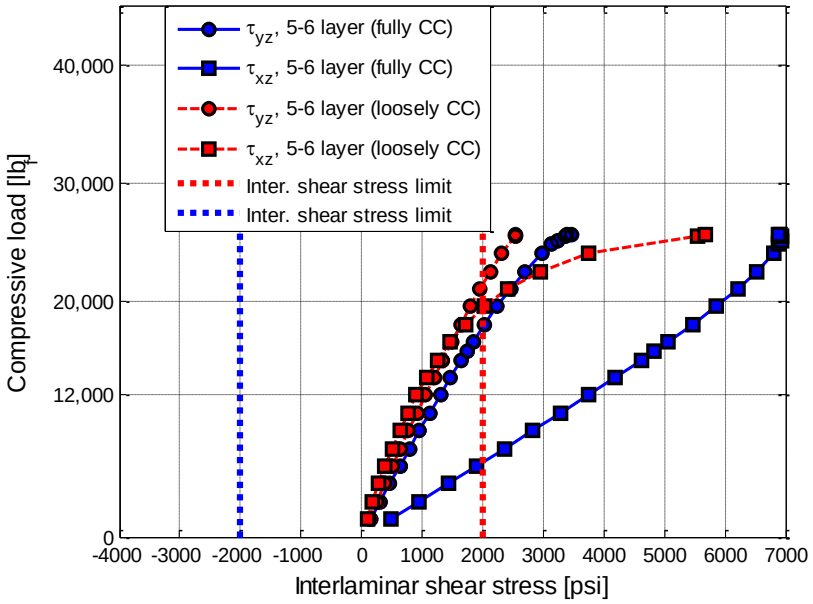

(a) Initial design

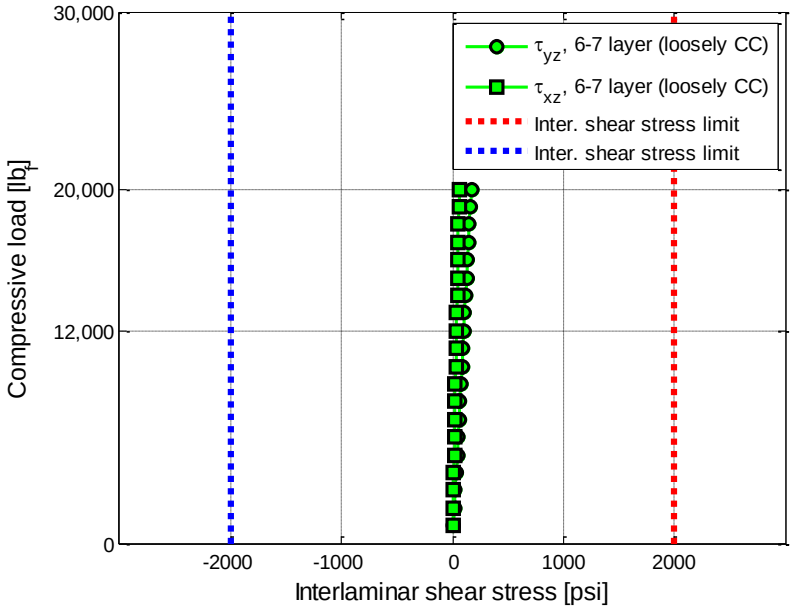

(b) Post-optimization

Figure B. 4. Concept 2: Interlaminar shear stress curves.

(c) Concept 3

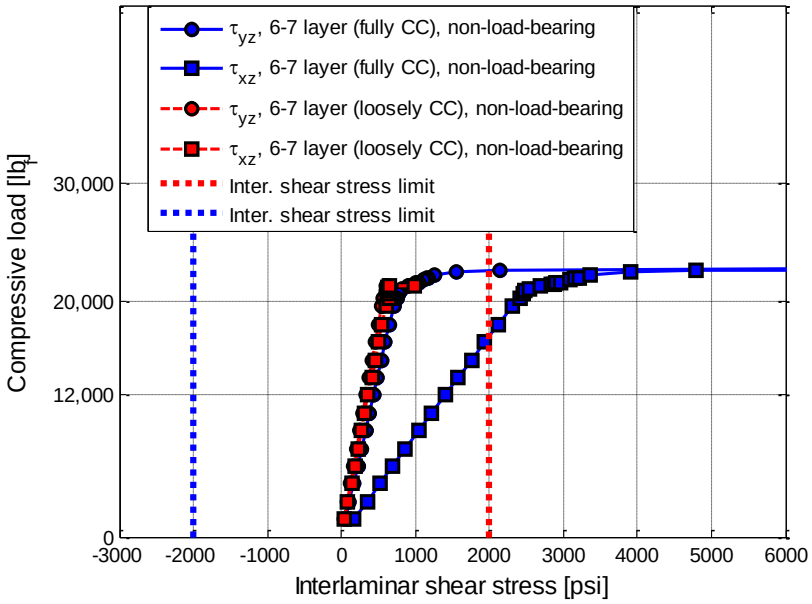

(a) Initial design

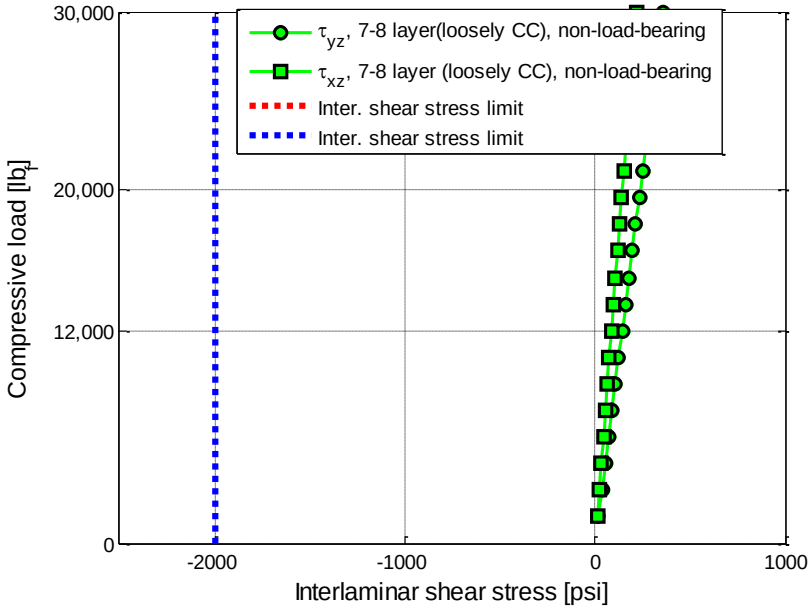

(b) Post-optimization

Figure B. 5. Concept 3: Interlaminar shear stress curves.

(d) Concept 4

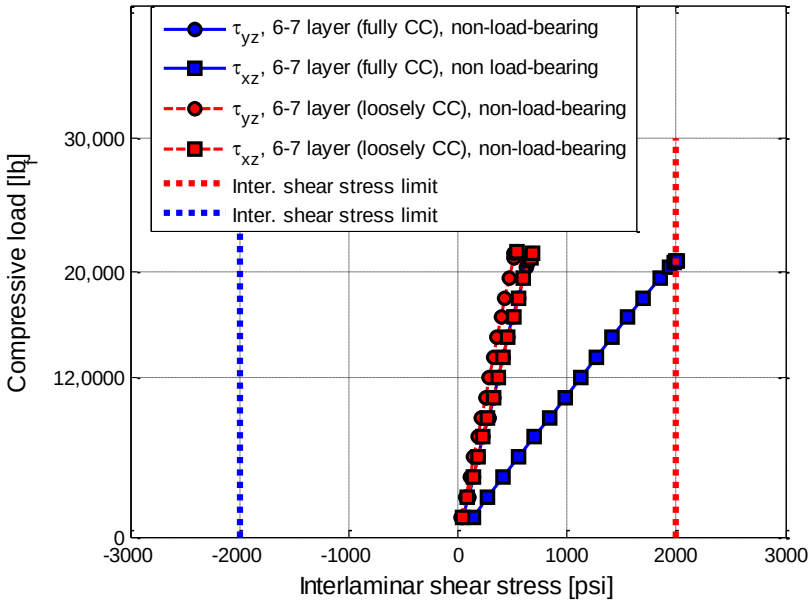

(a) Initial design

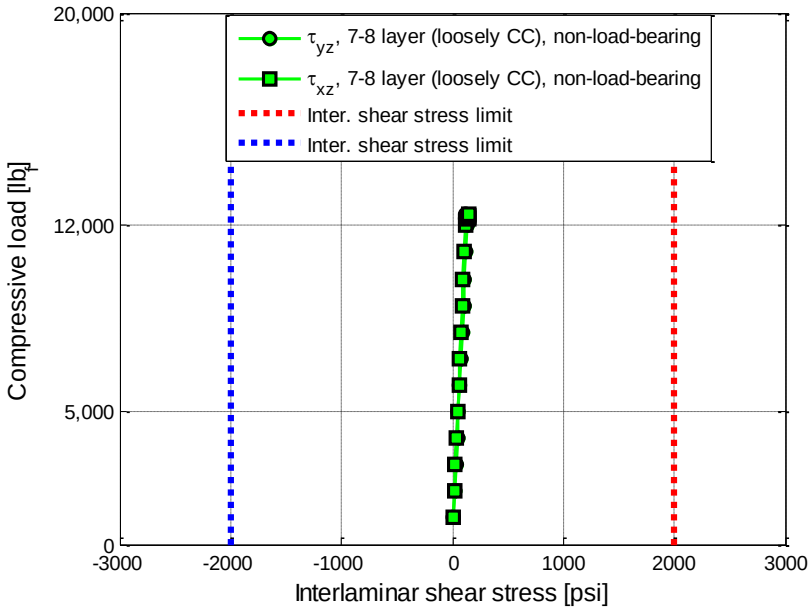

(b) Post-optimization

Figure B. 6. Concept 4: Interlaminar shear stress curves.